UTTAC-90, 2021

UTTAC

ANNUAL REPORT 2020

TANDEM ACCELERATOR COMPLEX
Research Facility Center for Science and Technology
University of Tsukuba

https://www.tac.tsukuba.ac.jp/

UTTAC

ANNUAL REPORT 2020

April 1, 2020 – March 31, 2021

UTTAC-90, 2021

Editors : Tetsuaki Moriguchi, Kimikazu Sasa, Yoshihiro Yamato, Masumi Matsumura, Masao Sataka, Hiroshi Naramoto, Eiji Kita, and Hiroshi Kudo (editor-in-chief)

UTTAC ANNUAL REPORT is a series of issues, which describes annual research activities at Tandem Accelerator Complex, Research Facility Center for Science and Technology, University of Tsukuba.

Tandem Accelerator Complex, Research Facility Center for Science and Technology,
University of Tsukuba
Tennodai 1-1-1, Tsukuba, Ibaraki 305-8577, Japan
annual@tac.tsukuba.ac.jp

Cover: SF_6 recirculation system of the UTTAC 6MV tandem accelerator. Since SF_6 gas used for electrical isolation of high voltage is a greenhouse gas, it must be recirculated without being released into the environment.

PREFACE

This annual report covers researches carried out at University of Tsukuba Tandem Accelerator Complex (UTTAC) during the fiscal year 2020 (1 April 2020 ~ 31 March 2021). The topics include not only accelerator-based researches using the 6MV Pelletron and 1MV Tandetron accelerators, but also radioisotope-based researches employing positron annihilation spectroscopy and Mössbauer spectroscopy. Notably, the activity in research and education in FY2020 was seriously influenced by COVID-19. To our regret, we had no visitors of high school students in FY2020. We hope such undesired situation will be resolved sooner or later.

September 1, 2021
Editorial board

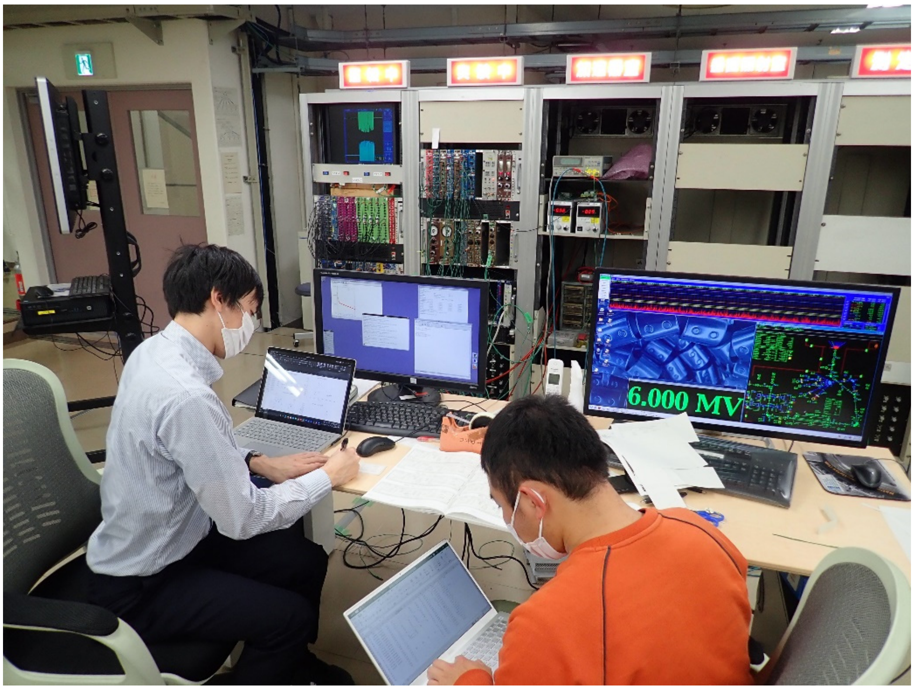

Graduate students performing experiments using the 6MV tandem accelerator.
Experimenters at UTTAC are obliged to wear masks until COVID-19 is gone.

CONTENTS

1. ACCELERATOR AND RELATED FACILITIES

2. NUCLEAR AND ATOMIC PHYSICS

3. ACCELERATOR MASS SPECTROMETRY

4. ION-BEAM APPLICATIONS

5. ISOTOPE APPLICATIONS

6. BEAM IRRADIATION EFFECT

7. LIST OF PUBLICATIONS AND PRESENTATIONS

1.

ACCELERATOR AND RELATED FACILITIES

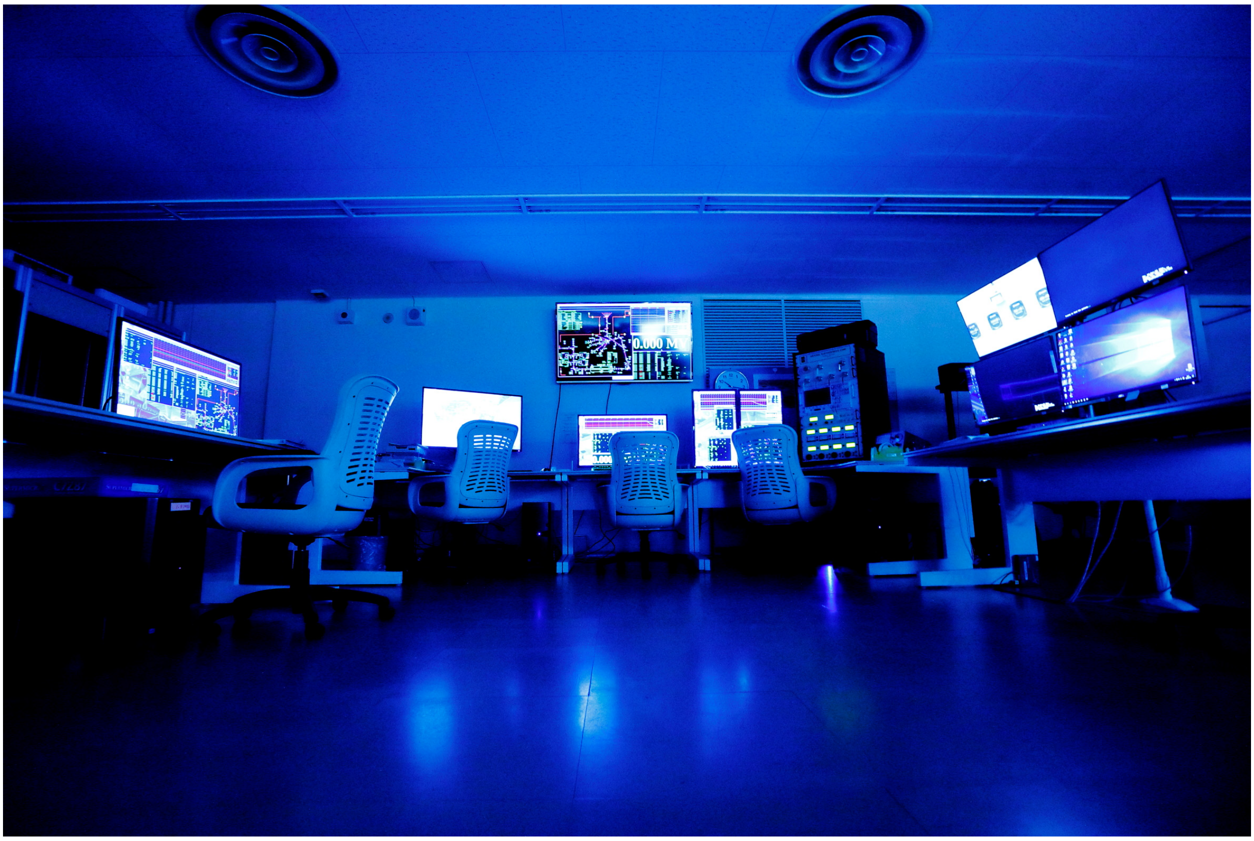

Control area of the UTTAC 6MV tandem accelerator

1.1 Accelerator operation FY2020

K. Sasa, S. Ishii, Y. Tajima, T. Takahashi, Y. Yamato, M. Matsumura, T. Moriguchi

The University of Tsukuba, Tandem Accelerator Complex (UTTAC) is promoting the maintenance and operation of a combined tandem accelerator facility consisting of the 6MV Pelletron tandem accelerator and the 1MV Tandetron accelerator for cooperative researches both inside and outside the University. The accelerator operations were suspended from April 16th to May 17th, 2020, in response to the state of emergency for the COVID-19 infection. UTTAC has undertaken a variety of countermeasures to prevent the spread of COVID-19. However, some outside users refrained from accelerator experiments in fiscal 2020. The operating time of the 6MV Pelletron tandem accelerator decreased by about 28% compared to fiscal 2019 [1].

We renewed one monitoring post for neutrons in June, 2020. In addition, a chiller for cooling water was replaced by a new one in August, 2020. We had a periodic inspection for the radiation facility in the Radiation Hazard Prevention Act once 5 years in December, 2020. The terminal potential stabilizer (TPS) for the 6MV Pelletron tandem accelerator was broken in March, 2021. We repaired an electronic circuit in the TPS before FY2021 started.

1 MV Tandetron accelerator

The 1MV Tandetron accelerator has 2 negative ion sources and 4 beamlines. The operating time and the experimental beam time of the 1 MV Tandetron accelerator were 491.5 and 191.9 hours, respectively, during the total service time in fiscal 2020. The total number of operation days was 51. A total of 26 research programs was carried out and a total of 117 researchers used the 1 MV Tandetron accelerator. Figures 1 and 2 show classification of the accelerated ions and of the experimental purposes, respectively. This accelerator was maximally used for the biomedical research which occupied 41% of the beam time.

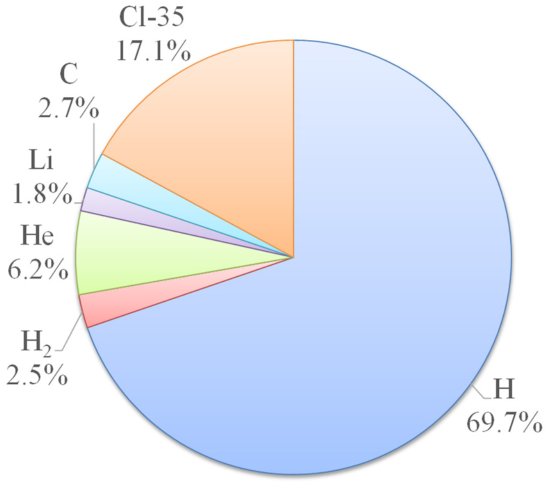

Fig. 1. Accelerated ions by the 1MV Tandetron accelerator in fiscal 2020.

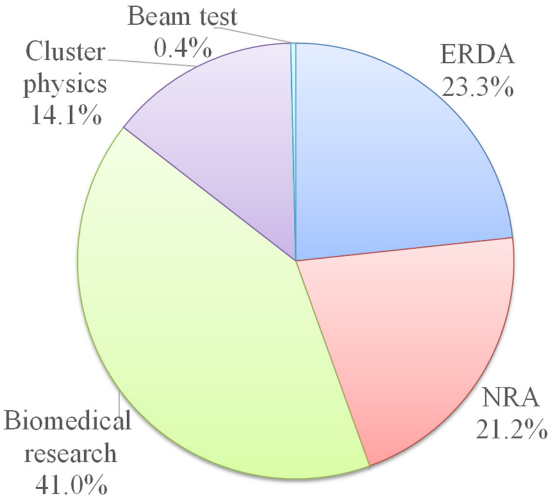

Fig. 2. Purpose of use of the 1MV Tandetron accelerator in fiscal 2020.

6 MV Pelletron tandem accelerator

The 6MV Pelletron tandem accelerator has 5 negative ion sources and 12 beamlines. The operating time and the experimental beam time of the 6 MV Pelletron tandem accelerator were 1054.5 and 811.4 hours, respectively, during the total service time in fiscal 2020. The total number of operation days was 100. A total of 44 research programs was carried out and a total of 295 researchers used the 6MV Pelletron tandem accelerator. Figure 3 shows the beam time histogram with respect to the terminal voltage. Figures 4 and 5 show classification of the accelerated ions and of the experimental purposes, respectively. The operating time at terminal voltages of 5 and 6 MV accounted for 84% of all the beam time. A deuteron beam was accelerated by the 6MV Pelletron tandem accelerator for the first time. This accelerator was used most often for AMS which occupied 49.3% of the beam time.

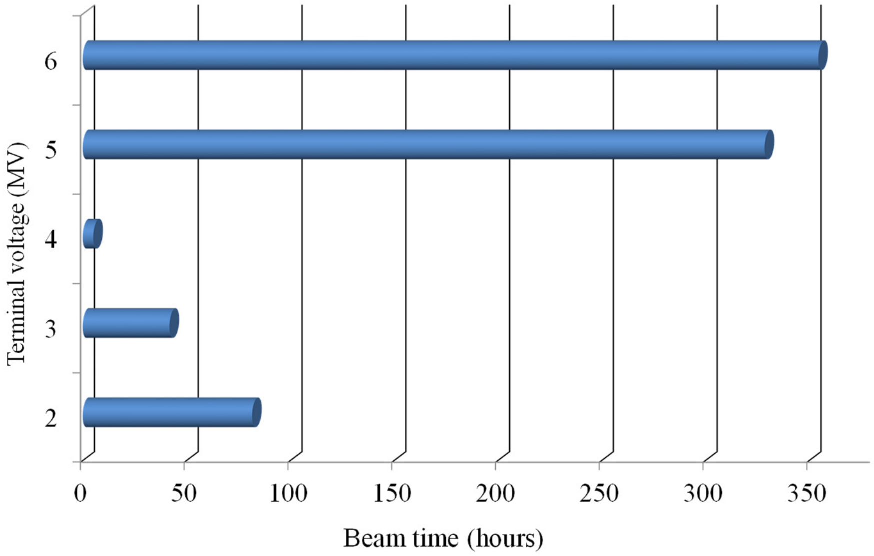

Fig. 3. Beam time histogram as a function of the terminal voltage for the 6MV Pelletron tandem accelerator in fiscal 2020.

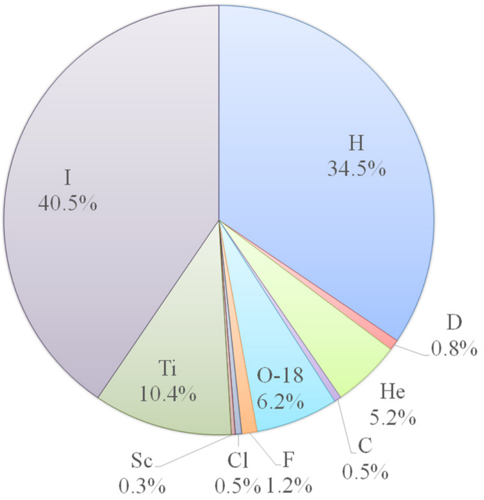

Fig. 4. Accelerated ions for the 6 MV Pelletron tandem accelerator in fiscal 2020.

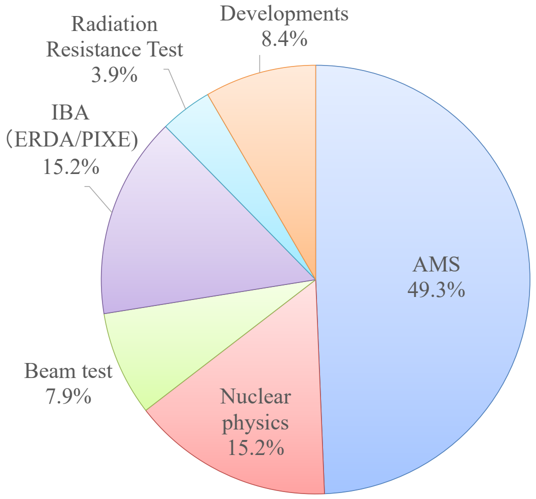

Fig. 5. Purpose of use of the 6 MV Pelletron tandem accelerator in fiscal 2020.

Reference

[1] K. Sasa et al., UTTAC Annual Report 2019, UTTAC-89 (2020) 1.

1.2 Current distribution measurement of accelerated ions from the 6MV tandem accelerator

M. Sataka, T. Takahashi, H. Naramoto, H. Kudo, K. Sasa

Acceleration tests of ion beams obtained from the 6MV tandem accelerator at UTTAC have been continued [1-4]. The experimental data of the highest energies of available ions is indispensable for radiation resistance tests of semiconductors used in space. While only weak beams are needed in the radiation resistance tests, the beam intensity is also important for ion beam modification of materials or micro-beam analysis of environmental samples.

In this fiscal year, Sc ion was newly tested, while Cl and Ti data were updated. We have measured beam currents of the accelerated ions as a function of the ion charge at an acceleration voltage of 1, 3, and 6 MV. Figure 1 shows the beam current distributions of Sc ion as a function of the ion charge at the maximum terminal voltage of 6 MV. Argon gas and a carbon foil were used as the strippers at the 6 MV terminal. The gas pressure was about 5 μPa, and the thickness of the carbon foil was about 5 μg/cm^2. The ion current distribution for the foil stripper shifts to higher charge state by about 3 than for the gas stripper.

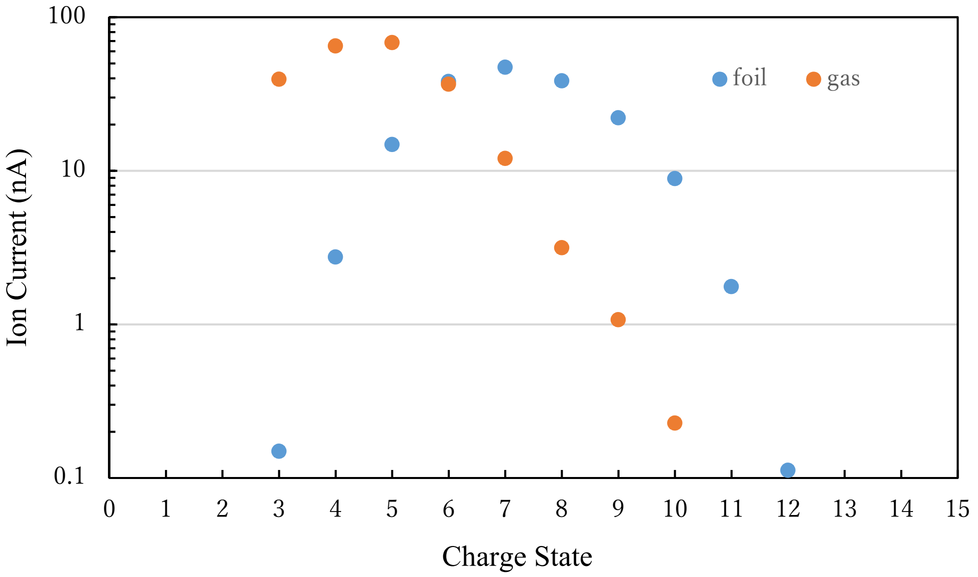

Fig. 1. Beam current distribution of Sc ions at the terminal voltage of 6 MV. Gas and foil strippers were used in the high voltage terminal.

We have tested negative molecular ion injection towards the high voltage terminal. In this year Sc and Ti were tested. For injection of molecular ions, the accelerated ion energy cannot be determined only by the terminal voltage and the ion charge after acceleration. The maximum acceleration energies obtained in this test using the foil stripper are 76.4 and 77.9 MeV for Sc and Ti ions, respectively.

Table 1 shows the beam current distributions of Sc and Ti ions, together with N, Al, Ca, Mo and W ions investigated previously. Table 2 shows the ion charges and maximum energies obtained for injection of negative atomic ion at the terminal voltage of 6 MV, which have been accumulated from 2016 to 2020.

Table 1. Beam current distributions for molecular ion injection at the terminal voltage of 6 MV, which have been accumulated since 2016. The measured beam intensity is shown by the symbols: ○: ≥ 1nA, △: ≤1nA. The data shown in red were obtained using the foil stripper.

charge state	N	Al	Ca	Sc	Ti	Mo	W
14							
13					△		
12				△	○		
11				△	○		△
10			△	○	○	△	△
9			△	○	○	○	○
8		○	△	○	○	○	○
7		○		○	○	○	
6	△	○	△	○	○	○	
5	○	○	△	○	○	○	
4	○			○	○	○	
3	○			○	○		
2	○						
1							

Table 2. Summary of the acceleration tests from 2016 to 2020 for negative atomic ion injection at the terminal voltage of 6 MV. The measured beam intensities are shown by the symbols: ○: ≥ 1nA, △: ≤1nA. The data shown in red were obtained using the foil stripper.

charge state	energy (MeV)	H	He	Li	B	C	O	F	Al	Si	S	Cl	Ni	Cu	Br	Ag	I	Au
14	90														△	△	○	△
13	84													△	△	△	○	△
12	78												△	○	○	○	○	○
11	72										△	△	○	○	○	○	○	○
10	66									○	○	○	○	○	○	○	○	○
9	60								△	○	○	○	○	○	○	○	○	○
8	54						○	○	○	○	○	○	○	○	○	○	○	○
7	48						○	○	○	○	○	○	○	○	○	○	○	
6	42					○	○	○	○	○	○	○	○	○	○	○		
5	36				○	○	○	○	○	○	○	○	○	○	○	○		
4	30				○	○	○	○		○	○	○	○	○	○			
3	24			○	○	○	○	○		○	○	○	○					
2	18		○	○	○	○	○	○			○	○						
1	12	○	○	○														

References

[1] M. Sataka et al., UTTAC Annual Report 2016, UTTAC-86 (2017) 9.

[2] M. Sataka et al., UTTAC Annual Report 2017, UTTAC-87 (2018) 5.

[3] M. Sataka et al., UTTAC Annual Report 2018, UTTAC-88 (2019) 5.

[4] M. Sataka et al., UTTAC Annual Report 2019, UTTAC-89 (2020) 3.

1.3 Measurement of air dose rate with proton and deuteron beams

T. Moriguchi, M. Matsumura, K. Sasa, S. Ishii, T. Takahashi, Y. Yamato

In accelerator facilities, it is necessary to manage the air dose rate during beam irradiation. In particular, care must be taken for accelerating proton or deuteron by the 6 MV Pelletron tandem accelerator at UTTAC because air dose rates during their irradiation are much higher than those of other ion species. The reason is that the maximum beam energy per nucleon is realized for proton, while the binding energy of deuteron is small compared with that of other nuclei. From the point of the radiation safety, we have measured air dose rates during acceleration of proton and deuteron since last FY. The details of measurement are described in Ref. [1]. As shown in Fig. 1, air dose rates were measured by three pairs of area monitors for gamma-ray (DAM-102, Hitachi Ltd.) and neutron (DAM-251, Hitachi Ltd.). Tantalum (Ta) and carbon (C) were used as beam stoppers. Carbon stopper C1 shown in Fig. 1 is located inside the shielding wall at 425 mm from the wall surface in the vertical line room.

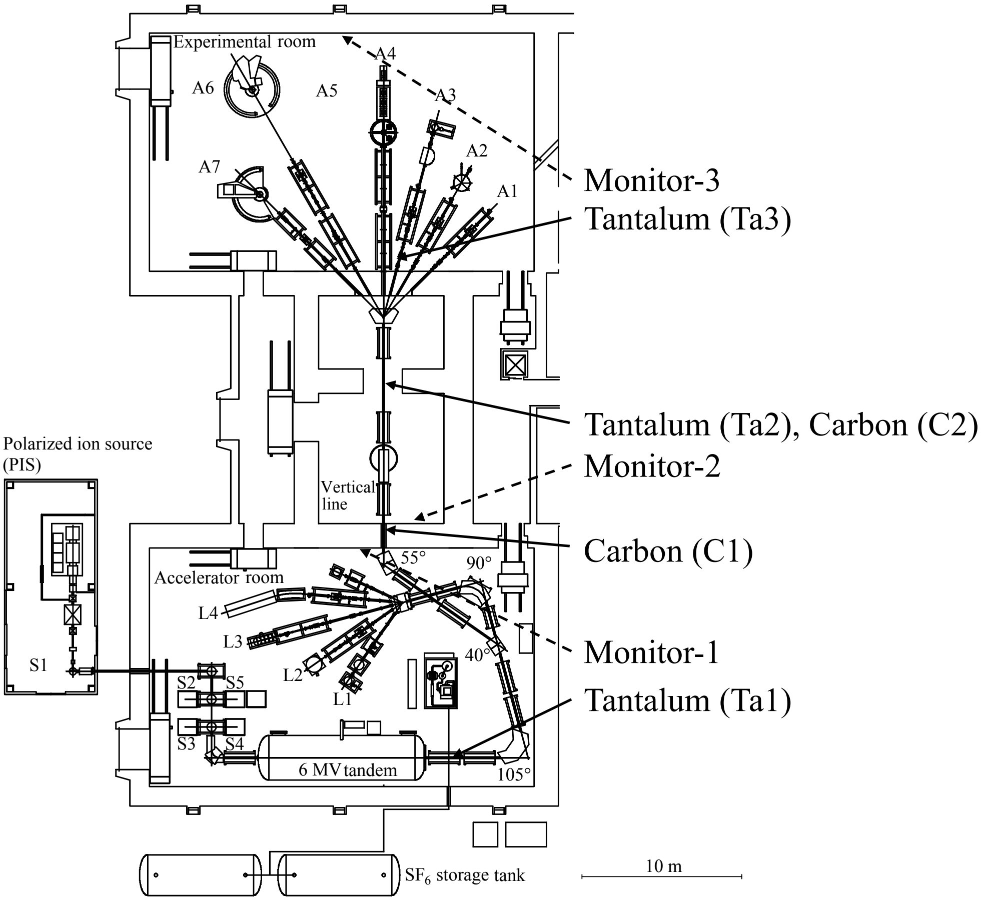

Fig. 1. Layout of the 6 MV Pelletron tandem accelerator facility. Solid arrows indicate the positions of beam stoppers: tantalum (Ta1, Ta2, and Ta3) and carbon (C1 and C2). Dashed arrows indicate the positions of three pairs of area monitors for gamma-ray and neutron (Monitor-1, Monitor-2, and Monitor-3).

Figure 2 shows the measured air dose rates as a function of beam energy during irradiation of the beam stoppers with proton and deuteron beams, together with the last FY's results. Note that the beam current is approximately 300 nA for proton and 30 nA for deuteron which are equal to one-tenth of the certificated limitation. As shown in Fig. 2 (b), air dose rates of both gamma-ray and neutron for the tantalum stopper are lower than those for the carbon stopper except for that of neutron during proton irradiation at 10 and 12 MeV. This result suggests that carbon is an effective stopper for proton beam to reduce air dose rate of neutron. When the 12 MeV proton beam impinges on the carbon stopper inside the shielding wall (C1), the air dose rates measured by Monitor-2 are several μSv/h for both gamma-ray and neutron. For carbon stopper during deuteron irradiation, the dip around 10 MeV is seen in both gamma-ray and neutron, but the reason for this is not clear at the moment. We will continue to measure the air dose rate and improve the management system for radiation safety at UTTAC.

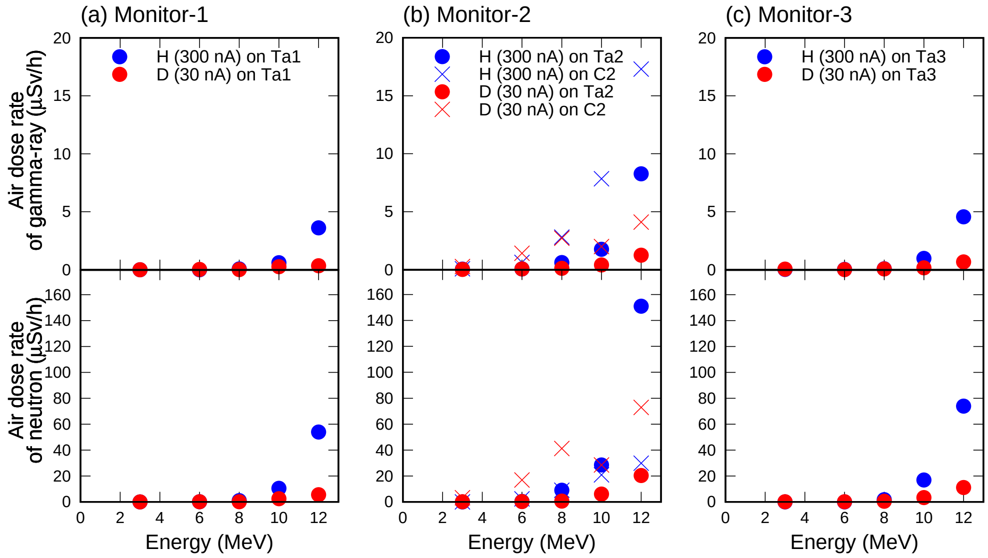

Fig. 2. Air dose rates of gamma-ray (upper panels) and neutron (lower panels) measured by (a) Monitor-1, (b) Monitor-2, and (c) Monitor-3. These results were obtained by the nearest area monitor to the irradiated stopper. Blue and red symbols represent the results for proton (H) of approximately 300 nA and deuteron (D) of approximately 30 nA, respectively. Circles and crosses represent the results for tantalum (Ta1, Ta2, and Ta3) and carbon (C2) stoppers, respectively. Note that backgrounds were already subtracted.

Reference

[1] T. Moriguchi et al., UTTAC Annual Report 2019, UTTAC-89 (2020) 5.

2.

NUCLEAR AND ATOMIC PHYSICS

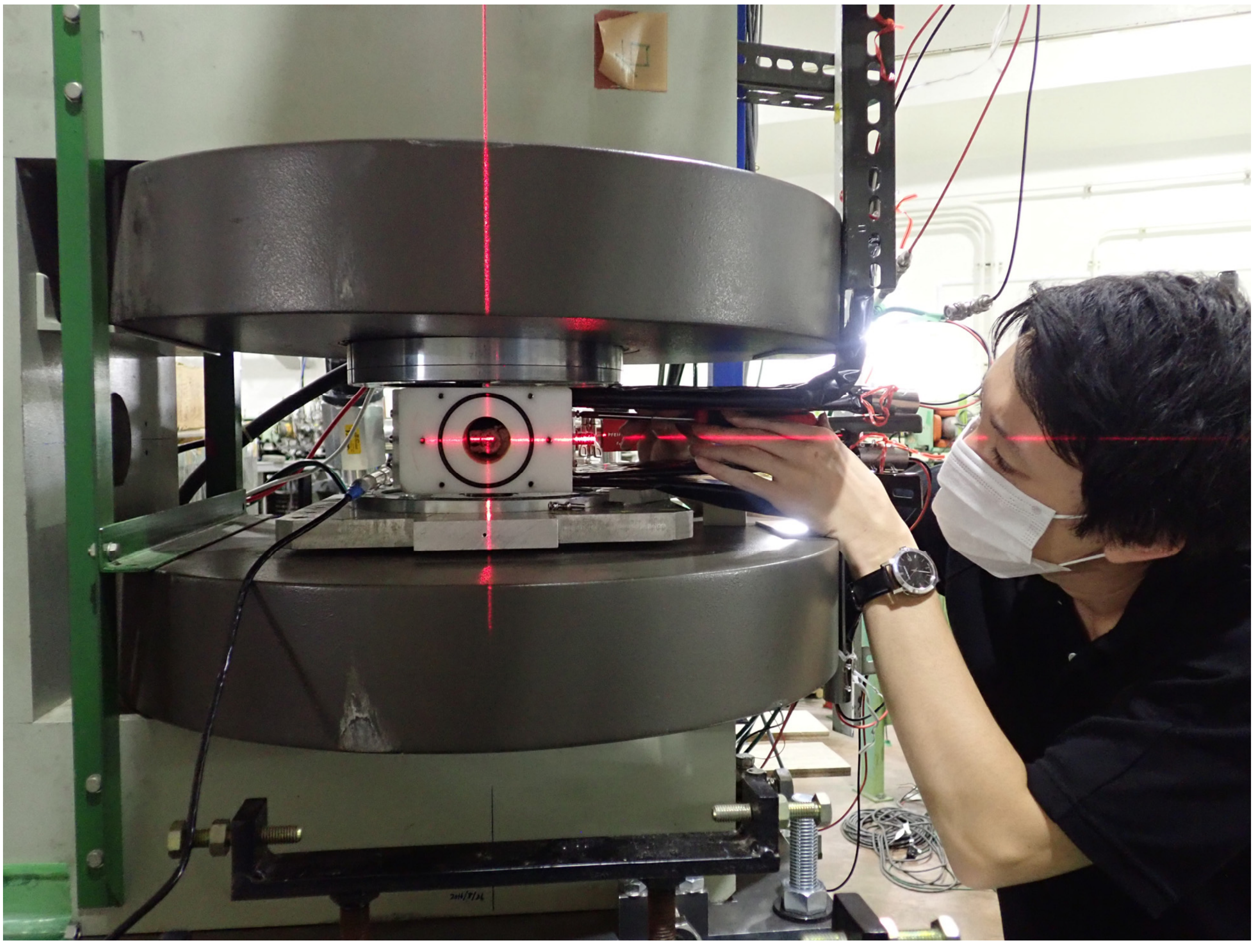

Setup for measurements of nuclear magnetic moment

2.1 Measurement of the sign of nuclear moment for unstable nucleus ^{29}P by using rotating magnetic field

A. Ozawa, K. Tomita, T. Moriguchi, Y. Yamato, N. Kaname, M. Hayashi, A. Yano

We developed rotating magnetic field system to determine the sign of nuclear magnetic moments (μ's) for unstable nuclei [1]. In FY2020, we have succeeded in determining the sign of μ for ^{29}P ($I^{\pi}=1/2^{+}$). Up to now, although the absolute value of μ for the nucleus is determined ($|\mu|=1.2349(3)$), the sign of μ is unknown [2]. In this report, we briefly present the result.

Our rotating magnetic field system is shown in Fig. 1 in Ref. [3]. In the present work, instead of the phase shifter, variable cable delay was applied. The direction of rotating magnetic field is defined by the direction of the static magnetic field (H_0) as shown in Ref. [1]. If NMR asymmetry disappears by applying right-circularly RF field, the sign of μ is positive [3]. In the present work, the polarized ^{29}P was produced by using a 12 MeV polarized proton beam and a 0.5 mm thick Si target (p-High) [4, 5]. We applied H_0=1.647 kG. In this case, Larmor frequency of μ for ^{29}P is about 3.1 MHz, corresponding to about 320 ns revolution time. In the rotating magnetic field system, we fixed the two RF fields to 3.10±0.05 MHz. and measured the NMR asymmetry by changing the cable delay. Observed cable delay dependence of the NMR asymmetry is shown in Fig. 1. Experimental NMR asymmetry disappears at around 50 ns delay. In the offline measurement, by using pick-up coils, we confirmed that when 80 ns delay is applied, right-circularly RF field is produced. Although there is slight difference of the delay between online and offline results, the present results show that the sign of μ for ^{29}P is positive. The positive sign is consistent with prediction by the Schmidt value ($\mu=+2.7926$ n.m.) for the nucleus (odd Z, $l=0$).

In further studies, we will apply the present system to determination of the sign of μ for the nuclei, for which only absolute values are known.

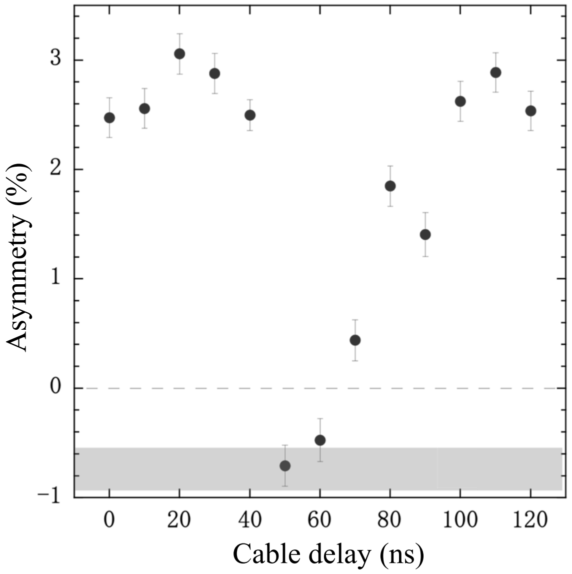

Fig. 1. Observed cable delay dependence of NMR asymmetry. Grey region shows the NMR asymmetry without RF field.

References

[1] D. Nagae et al., UTTAC Annual Report 2013, UTTAC-83 (2014) 12.

[2] N. J. Stone, At. Data Nucl. Data Tables 90 (2005) 75.

[3] D. Nagae et al., UTTAC Annual Report 2012, UTTAC-82 (2013) 7.

[4] A. Ozawa et al., UTTAC Annual Report 2018, UTTAC-88 (2019) 7.

[5] A. Ozawa et al., UTTAC Annual Report 2019, UTTAC-89 (2020) 7.

2.2 A study of $\vec{p}$ + $^{\text{nat.}}$Si reaction by the 6 MV tandem accelerator

A. Yano, A. Ozawa, T. Moriguchi, Y. Yamato, K. Tomita, N. Kaname, M. Hayashi

It is important to measure nuclear magnetic moments (μ) since they reflect the nuclear shell structure. In particular, if μ in the pair of mirror nuclei are measured, we can calculate their expectation values of angular momentums. Our group has been measuring μ of ^{30}P, which is self-mirror nucleus (N=Z), by using the nuclear magnetic resonance method observing β-ray emission asymmetry (β-NMR). In this FY, to optimize experimental conditions of β-NMR, we measured the energy and target dependences of yield and β-NMR effect for ^{29}P. Since the proton number of ^{29}P is the same as that of ^{30}P, hyperfine interaction of ^{29}P with target is equal to that of ^{30}P.

Experimental setup is similar to that of the previous β-NMR measurement [1]. In order to confirm the production of ^{29}P, we irradiated a 0.5 mm thick wafer of Si with a 12 MeV polarized proton beam. Figure 1 shows the typical time spectrum of counted β-ray. Solid lines indicate fitting results taking into account the life times of ^{29}P, ^{30}P, and ^{25}Al. These results imply that the production of ^{29}P is confirmed in this study. By integrating the spectra for the nuclei, we deduced the yields of the nuclei.

The beam energy dependences of yields for ^{29}P and ^{30}P via $\vec{p}$ + $^{\text{nat.}}$Si reaction are shown in Fig. 2. The yield of β-ray in Fig. 2 is normalized by the beam current. The yield of ^{29}P increases as the beam energy increases from 6 to 12 MeV. This result suggests that 12 MeV polarized proton is suitable for the β-NMR measurements for ^{30}P.

As shown in Fig. 3, the energy dependence of asymmetry which is proportional to a nuclear spin polarization is not seen clearly. The statistical error around 6 and 8 MeV is due to the low beam intensity. Consequently, we conclude that 12 MeV is the optimum energy for β-NMR measurement of ^{30}P in terms of yield and β-

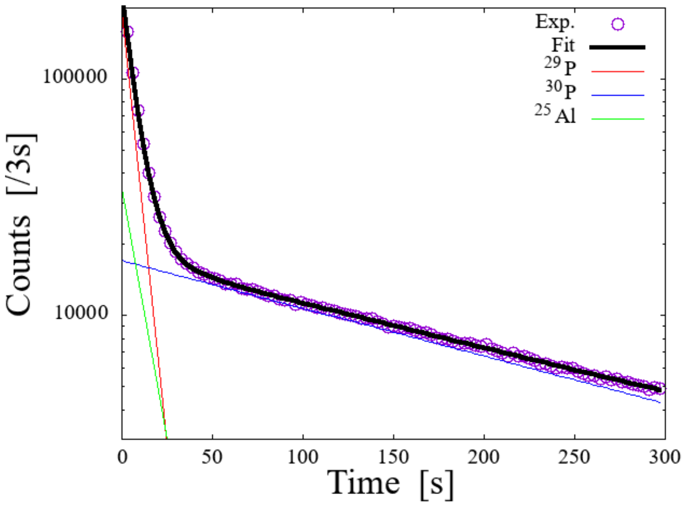

Fig. 1. Typical time spectrum of the observed β-ray.

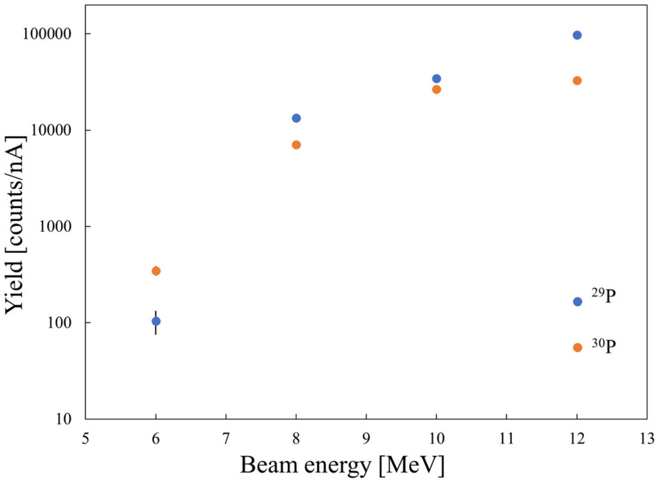

Fig. 2. Yields of ^{29}P and ^{30}P as a function of polarized proton energy.

NMR effect.

To make a suitable choice of Si-containing target, β-NMR effect measurements of ^{29}P were performed with Si, SiO_2 and SiC. These materials contain $^{nat.}$Si and are crystalline structures. Considering a difference in symmetry of crystal structure, we prepared two kinds of SiO_2 crystals. One has a Z-cut surface which is expressed as (0 0 0 1) in Miller index, meaning that its surface is perpendicular to Z axis of the crystal structure. Another has an X-cut (2 −1 −1 0) surface perpendicular to X axis. We observed large β-NMR effect of ^{29}P only for Si. In this viewpoint, using a Si target is appropriate for β-NMR measurements of ^{30}P.

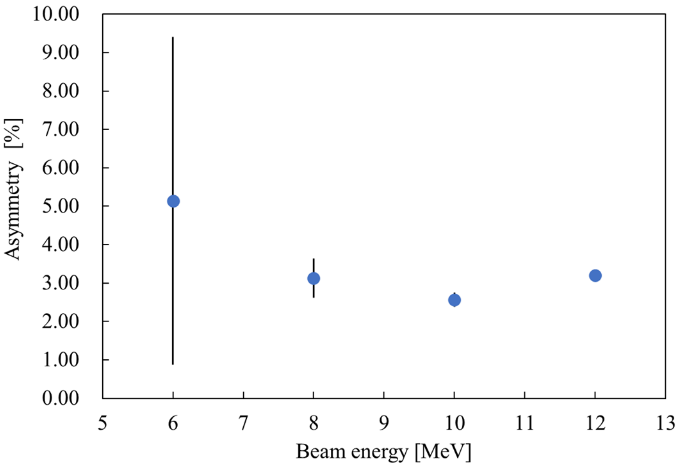

Fig. 3. Measured asymmetry of ^{29}P β-NMR as a function of the beam energy.

It is reported that β-NMR effect with a Si target is influenced by the electric field gradient in the lattice of Si crystal [2]. We need to consider this effect in future experiments.

References

[1] A. Ozawa et al., UTTAC Annual Report 2017, UTTAC-87 (2018) 7.

[2] W. Seelinger et al., Nucl. Instr. Meth. Phys. Res. B 63 (1992) 173.

2.3 Production of high intensity spin polarized ^{19}O for materials science applications

M. Mihara[1], Y. Otani[1], Y. Kimura[1], M. Fukuda[1], K. Matsuta[1], H. Ishiyama[2], T. Moriguchi, K. Tomita,
A. Yano, A. Ozawa

Solid oxide fuel cells (SOFC) are attracting much attention as clean energy systems with potential to generate a large amount of energy [1]. The ^{17}O (I = 5/2) nuclear magnetic resonance (NMR) is an important method for investigating the oxygen ion conductivity in SOFC materials [2]. However, the natural abundance of the ^{17}O isotope is only 0.038%, which becomes a bottleneck of ^{17}O NMR studies, because expensive samples enriched with ^{17}O are required to detect NMR signals. In this situation, a short-lived unstable nucleus ^{19}O ($T_{1/2}$ = 26.9 s, I = 5/2) is one of the alternative oxygen NMR probes to the stable ^{17}O nucleus. The β-ray detected NMR (β-NMR) technique using short-lived radioisotopes has been applied to various materials science studies. The β-NMR of ^{19}O in the SOFC materials does not require enriched samples, which will significantly reduce the cost and process of preparing samples. Previously, spin polarization of ^{19}O in the low energy nuclear reaction ^{18}O (d, p) ^{19}O has been studied [3] and then, the nuclear magnetic dipole (μ) and electric quadrupole (Q) moments have been precisely determined [4]. In the present study, we have tried to produce spin polarized ^{19}O via the inverse kinematics reaction d (^{18}O, ^{19}O) p, in order to utilize ^{19}O as an oxygen NMR probe nucleus for the study of SOFC materials.

The experiment was performed at the A7 course of the UTTAC facility. The experimental setup is shown in Fig. 1. A 30-MeV ^{18}O^{4+} beam provided by the 6-MV tandem accelerator impinged on a deuterium absorbed Ti (TiD$_x$; x ~ 1) foil with a thickness of 1 μm. The ^{19}O nuclei were produced through the d (^{18}O, ^{19}O) p reaction and implanted into a catcher sample CaO or TiO$_2$. The emerging angle of ^{19}O was selected to be about 5° where the maximum spin polarization of about 3% is expected from the previous study on the ^{18}O (d, p) ^{19}O reaction [3]. The sample within a cylindrical vacuum chamber was placed inside a Halbach array permanent magnet (SuperMagnetMan HB0080) which generates a magnetic field B ~ 0.5 T. The Halbach magnet has a doughnut shape with the outer and inner diameters of 84 mm and 40 mm, respectively, and the thickness of 25 mm. The spot size of the collimated ^{19}O ions was about 4×10 mm^2 at the sample position where the field inhomogeneity became a few %. A radio frequency (rf) coil was also set in the vacuum chamber to induce

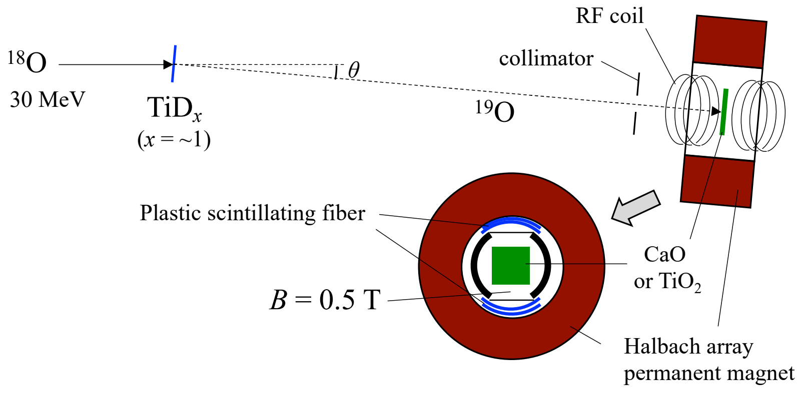

Fig. 1. Experimental setup.

---

[1] Department of Physics, Osaka University
[2] RIKEN Nishina Center for Accelerator-Based Science

NMR. Two sets of β-ray counter telescopes were placed between the chamber and the inner space of the magnet. Each telescope consists of two layers of a plastic scintillation fiber (Kuraray SCSF78-1.00mm-D) array, which was optically connected to a 16 ch multi pixel photon counter (MPPC) array (Hamamatsu C13368-3050EA-16) through optical fiber.

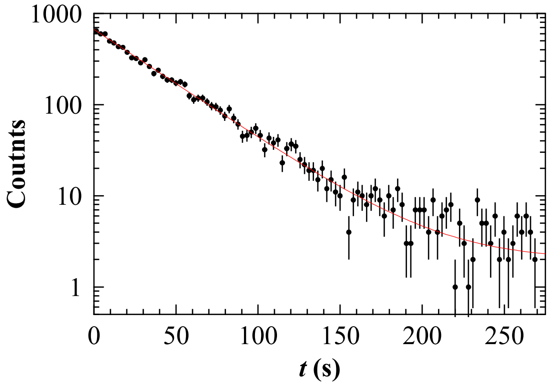

Fig. 2. β-ray time spectrum from a catcher material after irradiation of a 30-MeV ^{18}O beam on a TiD$_x$ target.

Figure 2 shows a typical β-ray time spectrum after irradiation of the $^{18}O^{4+}$ beam with an intensity of 400 nA. The spectrum is well explained by the halflife of ^{19}O with $T_{1/2}$ = 26.9 s [5]. The β-NMR measurement was performed by applying an rf field with the frequencies at around 2.4 MHz, the Larmor frequency at B = 0.52 T which is the calibrated value at the center of the magnet. However, no significant resonance was observed. Although the reason is not clear, the following two points should be considered. One is the misalignment of the sample along the beam axis, which might have caused mismatch of the NMR condition. The other is the capture of unpolarized electron(s) in the target, which reduces nuclear spin polarization during flight due to the hyperfine interaction. We are planning further measurements after improvement of the setup by adding a guiding field and a tilted foil stack to maintain and enhance ^{19}O nuclear polarization.

References

[1] H. Iwai et al., Transactions of the JSME 111 (2008) 13.
[2] T. Viefhaus et al., Solid State Ionics 177 (2006) 3063.
[3] K. Matsuta, et al., Nucl. Instr. Meth. Phys. Res. A 402 (1998) 229.
[4] T. Minamisono et al., Phys. Lett. B 457 (1999) 9.
[5] "Table of Isotopes CD ROM Edition" Edt. R. B. Firestone and V. S. Shirly, Wiley-Interscience (1996).

2.4 Performance test of low-pressure MWDC with 1/3-cell staggered layers

S. Y. Matsumoto[1,2], A. Sakaue[3], K. Itahashi[2], T. Moriguchi, T. Nishi[2], R. Sekiya[1,2], R. Tsuji[1], T. Uesaka[3]
K. Yako[2], J. Zenihiro[1]

In December 2020, we conducted a performance test of a new low-pressure multi-wire drift chamber (MWDC) using proton beams to evaluate tracking resolution, efficiency and the stability under a high-rate beam condition.

The MWDC has been developed mainly for two experiments at RIBF, RIKEN, search for double Gamow-Teller giant resonance (DGTGR) via $\left({}^{12}\mathrm{C}, {}^{12}\mathrm{Be}\left(0_2^+\right)\right)$ reaction [1] and systematic high-precision spectroscopy of pionic atoms (piAF) via $\left(d, {}^{3}\mathrm{He}\right)$ reaction [2]. In these experiments, the MWDC (i) should have high position resolution with good tracking efficiency for the precise spectroscopy, and (ii) should work under high rate background condition (an order of MHz triton in the DGTGR experiment and proton in the piAF experiment).

For these purposes, we developed new MWDCs with two features, namely low gas-pressure operation in the vacuum and novel plane configuration. The former feature is important in terms of suppression of the multiple scattering of the incident particles in the detector materials [3] and the latter contributes to achieve homogeneity of the spectral resolution by the 1/3-cell staggered three-layer structures (XX'X"(0°), UU'U"(+30°), VV'V"(−30°)). A typical MWDC is known to exhibit a non-negligible inhomogeneity in the spectra originating from an analytic bias in the proximity of wires [4, 5]. For each set of layers in the new MWDCs, we use two of the three layers by neglecting the one where the trajectory is closest to a wire.

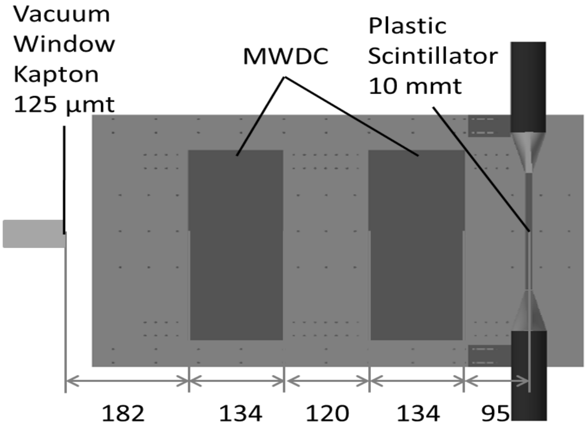

Fig. 1. Detector setup on the A7 beam line in UTTAC.

We performed the test experiment in 2.0 days at the A7 course in UTTAC, by using primary proton beams of 12 MeV/u. The beam was detected and identified by a plastic scintillator at the downstream of

---

[1] Department of Physics, Kyoto University
[2] RIKEN
[3] Center for Nuclear Study, University of Tokyo

the MWDCs as shown in Fig. 1. MWDC was operated with pure isobutane gas at 10 – 30 kPa.

The stability test of the MWDCs was conducted with around 10 kHz proton beams. This condition is comparable with the expected background in terms of the space charge effect. Under this severe condition, we verified that the detection efficiency does not change by more than a few percent.

From the above results, we found that the new MWDCs show satisfactory performance for our experiments.

References

[1] T. Uesaka et al., RIBF Proposal, No.141 (2015).
[2] K. Itahashi et al., RIBF Proposal, No.135 (2015).
[3] H. Miya et al., Nucl. Instr. Meth. Phys. Res. B 317 (2013) 701.
[4] T. Nishi et al., Phys. Rev. Lett. 120 (2013) 152505.
[5] Y. K. Tanaka, Ph. D. thesis, Univ. Tokyo (2016), Appendix B.

2.5 Measurement of convoy electron yield for atomic ions

S. Tomita, R. Suganuma, G. Kawasaki, S. Hatada

The main mechanism of radiation effects by fast charged particles is the energy transfer through the ionization of target materials, which leads to temperature increase along the trajectory of the incident particles. There is also a radiation effect through the chemical reaction caused by radicals which are produced by ionization of target materials and also by thermalized electrons. The radicals could play an essential role in the radiation effect, especially on a biological target, since Boudaïffa et al. [1] reported experimental results that show the resonant formation of the DNA strand break below 20 eV. Therefore, the energy distribution of low-energy scattered electrons could be crucial to understand the biological radiation effects. In the target material, such scattered electrons interact with the projectile ion [2-4]. Thus the energy distribution of scattered electrons is affected by the projectile ions. Such an effect would be most significant for the convoy electrons that are a part of secondary electrons emitted towards zero degrees with the same velocity as the projectile ions. To investigate the interactions of electrons with projectiles inside the target material, we plan to measure convoy electron yield for various ion beams. For this purpose, we have developed a zero-degree electron spectroscopy apparatus at a beamline of 1 MV Tandetron accelerator at UTTAC.

The schematic diagram of the experimental setup is shown in Fig. 1. An electrostatic energy analyzer located downstream of the thin target foil determines the kinetic energy of the electrons emitted towards zero degrees. Since the trajectories of analyzed electrons are affected by geomagnetism, we have built tri-axial square Helmholtz coils to generate a uniform magnetic field. A typical energy spectrum of secondary electrons is shown in Fig. 2. The apparent peak of convoy electron is observed at 160 eV which is equal to the kinetic energy of electron with the same velocity as the projectile ion of 0.29 MeV H^+. In Fig. 3, the electron yield at the peak position is shown in a two-dimensional plot as a function of the electric current on the square Helmholtz coil in the x (horizontal) and y (vertical) directions. The magnetic field at the maximum value of the convoy electron yields corresponds to the spatial position where geomagnetism is eliminated with the tri-axial square Helmholtz coil. We plan to measure convoy electron yields with this apparatus for various ion beams, including cluster ion beams.

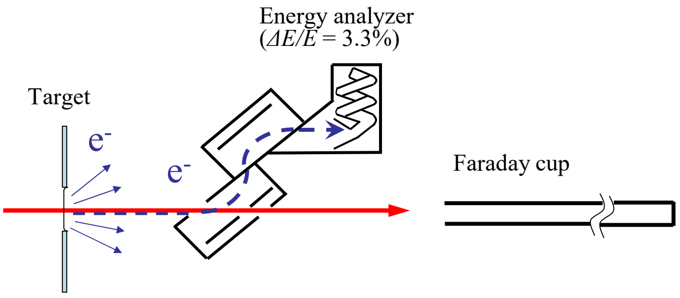

Fig. 1. Schematic diagram of the experimental setup.

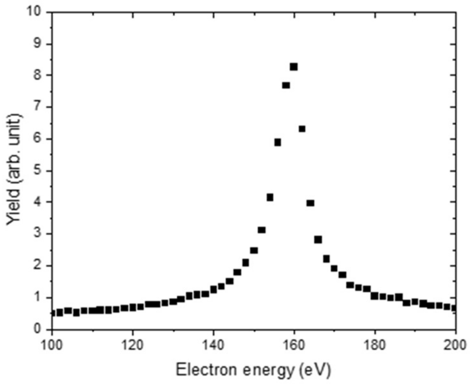

Fig. 2. Typical energy spectrum of convoy electrons from thin carbon foil of 4.9 μg/cm^2 for an incident beam of 0.29 MeV H$^+$.

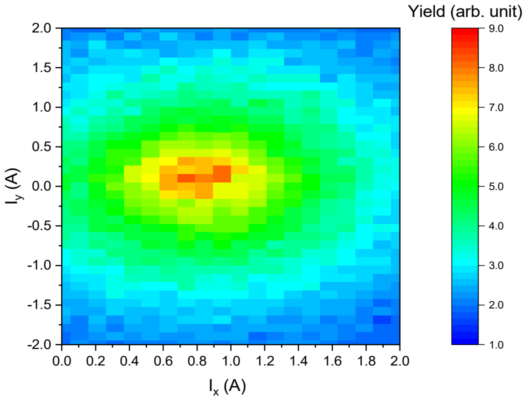

Fig. 3. The 2-dimensional plot of the yield of convoy electrons as a function of electric currents of horizontal (I_x) and vertical (I_y) magnet coils.

References

[1] B. Boudaïffa et al., Science 287 (2000) 1658.

[2] Y. Shiina et al., Nucl. Instr. Meth. Phys. Res. B 460 (2019) 30.

[3] S. Tomita et al., Nucl. Instr. Meth. Phys. Res. B 354 (2015) 109.

[4] S. Tomita et al., Phys. Rev. A 73 (2006) 060901.

3.

ACCELERATOR MASS SPECTROMETRY

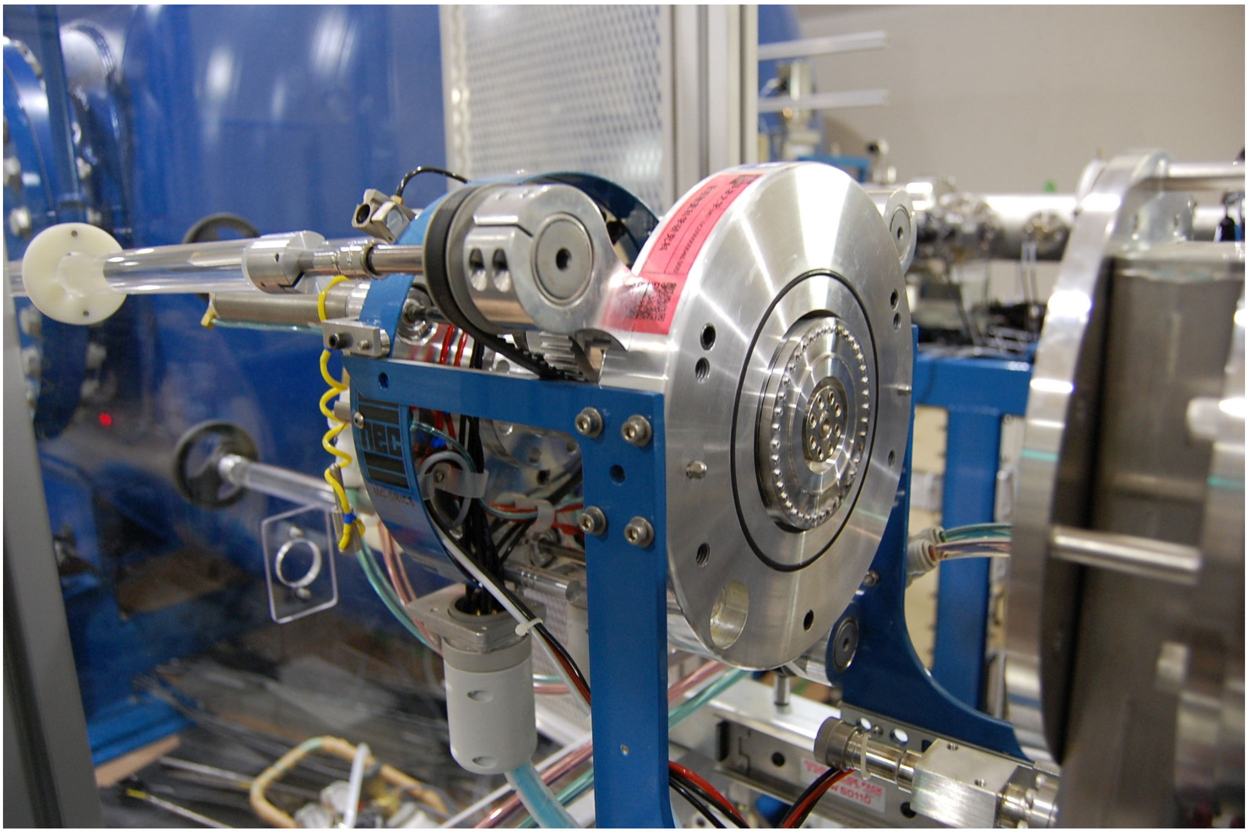

Negative ion source for AMS

3.1 Performance report of the Tsukuba 6 MV multi-nuclide AMS system in fiscal 2020

K. Sasa, T. Takahashi, M. Matsumura

The Tsukuba 6 MV multi-nuclide AMS system was operated for a total of 39 days and 400.4 hours in fiscal 2020. We measured 406 samples in total dealing with rare radionuclides such as ^{36}Cl and ^{129}I shown in Table 1. Figure 1 shows monthly-measured rare nuclides from April 2020 to March 2021.

Table 1. Number of measured ^{36}Cl and ^{129}I samples in fiscal 2020.

Item	Reagent & blank samples	Standard samples	Unknown samples	Total
Cl-36	9	7	13	29
I-129	71	53	253	377
Sub total	80	60	266	406

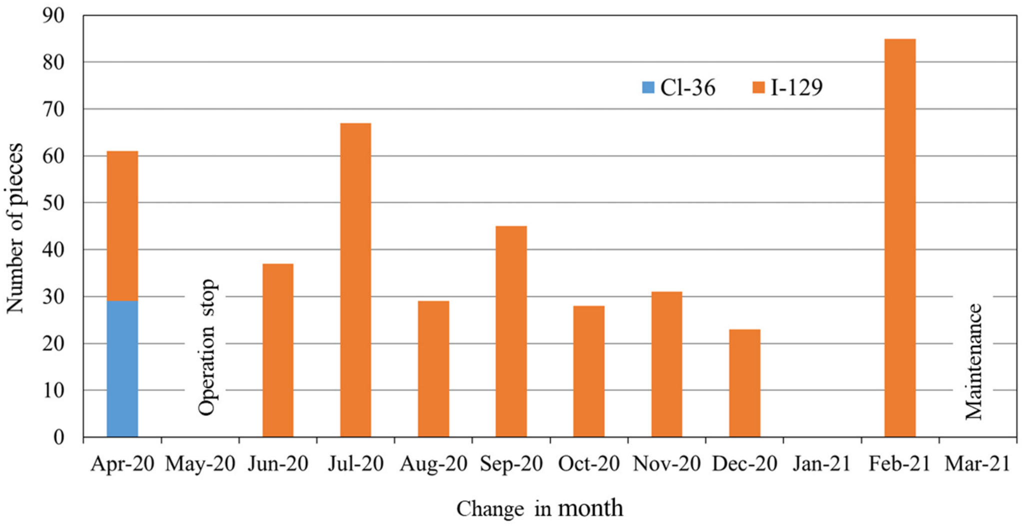

Fig. 1. Monthly-measured nuclides by the multi-nuclide AMS system from April 2020 to March 2021.

^{36}Cl-AMS

In fiscal 2020, ^{36}Cl analysis was applied for tracing cosmic ray events remaining in the ice-core. The DF2 ice-core samples were obtained from the DF station (77°19'S, 39°42'E, 3810 m above sea level) at Antarctica in 2007 [1]. The depth of interest was 239.5–242.0 m, corresponding to an age of 5494 BCE (+11 y/−15 y) to 5407 BCE (+11 y/−18 y) for the 5480 BCE cosmic ray event [2]. The ice-core was cut into 2.5-cm lengths. The average weight of each sample was 27 g. We merged five chlorine-fraction samples in order to resolve the ^{36}Cl analysis to 4–5 years, and spiked 2 mg of Cl carrier (NaCl supplied by Fisher Scientific, USA) for each sample. The chlorine fraction (cation-exchange eluate) was converted to AgCl for ^{36}Cl analysis. After the sulfur reduction, the dried AgCl was pressed into a copper cathode with an AgBr backing prepared under acid-aged conditions [3]. We measured ^{36}Cl/Cl background and ice-core samples with a total of 13 unknown samples under a beam condition of $^{36}\mathrm{Cl}^{8+}$ with 54.0 MeV (using a carbon foil stripper). The background ratios of $^{36}\mathrm{Cl/Cl} \sim 3 \times 10^{-15}$ were achieved with AgCl blank samples for ^{36}Cl AMS. The average concentration of ice-core samples was $(0.97 \pm 1.4) \times 10^{4}$ (atoms/g). As the result, there is no increase of ^{36}Cl concentrations in peak amplitude around the age of 5460 BCE.

^{129}I-AMS

The negative iodine ions (I^{-}) were extracted from an AgI sample and accelerated to 5 MeV in the first stage of the tandem accelerator and exchanged to the positive ions (I^{5+}) in an Ar gas cell for ^{129}I-AMS. After further acceleration to 30 MeV, $^{129}\mathrm{I}^{5+}$ was separated by high-resolution electric and magnetic analyzers before detection of the ion with a gas ionization detector. We used S-Purdue (Z94-0597) and S-Purdue2 (Z94-0596) reference materials ($^{129}\mathrm{I}/^{127}\mathrm{I}$ ratios of 8.38×10^{-12} and 6.54×10^{-11}) [4] as standards for normalization at UTTAC. The background ratios as low as $^{129}\mathrm{I}/^{127}\mathrm{I} \sim 2 \times 10^{-14}$ were achieved constantly with AgI chemical blank samples in fiscal 2020.

^{129}I was mainly measured at the AMS system in order to investigate the radioactive contamination in surface soils, water samples, and dissolved matters in river at Fukushima, and to trace the oceanic circulation with a total of 377 samples in fiscal 2020.

Reference

[1] H. Motoyama et al., Scientific Drilling 5 (2007) 41.
[2] F. Miyake et al., PNAS 114(5) (2017) 881.
[3] S. Hosoya et al., Nucl. Instr. Meth. Phys. Res. B 438 (2018) 131.
[4] P. Sharma et al., Nucl. Instr. Meth. Phys. Res. B 123 (1997) 347.

3.2 Measurements of ^{129}I in the Cooling Pond, Chernobyl

K. Nishizuka, A. Sakaguchi, V. Kanivetz[1], K. Sasa, T. Takahashi, M. Matsumura, S. Yamasaki, K. Sueki

An estimated amount of radionuclides in excess of 2000 TBq was accumulated in the Cooling Pond (CP) of the Chernobyl Nuclear Power Plant as a result of the nuclear accident [1]. The source of water for this pond is the Pripyat River, which runs just east of the CP and is geographically lower than the CP. Even after the reactors were closed, the water level in the pond was maintained by continuous pumping of water from the river so as to prevent environmental releases/dispersion of radionuclides due to the lowering of the water level in the cooling pond. However, the water level of the pond has been decreasing since 2014 as a result of the cessation of pumping caused by the deterioration of the political situation and of the warming/drying of the climate. In this study, we focused on the measurement of ^{129}I amount in the pond, which has not yet been evaluated. We also studied methods to accurately and precisely measure the total iodine concentrations in environmental water samples.

Water samples were collected in 2018-2020 at the sites N, NW, W, SW and S in the CP at some depths (Fig. 1). The collected water and pore water samples from the sediments were filtered through a 0.45 µm pore size filter, and a few grams of each sample was sub-sampled for ion chromatography to determine the levels of dissolved major cations and anions. Dissolved ^{137}Cs was quantified with a Ge semiconductor detector, and ^{90}Sr was chemically separated and its progeny ^{90}Y was quantified with a liquid scintillation counter. For the measurement of inorganic ^{129}I, target samples were prepared as AgI precipitates after purification of the iodine using an appropriate amount of sample water. The ^{129}I/^{127}I atom ratios in the samples were measured by the AMS system at UTTAC, and the ^{127}I concentrations were measured by ICP-MS (Agilent 8800) using ^{185}Re as an internal standard. As a preliminary experiment for the determination of 'total iodine' in natural water samples, including inorganic iodine and organic iodine, we determined recovery rates of I^-, IO_3^- and organic-I (γ-globulin) in trap-solutions obtained from the pyrohydrolysis method. In these experiments, a standard IO_3^- solution was prepared from the I^- standard solution, using radioactive iodine ^{125}I as a tracer.

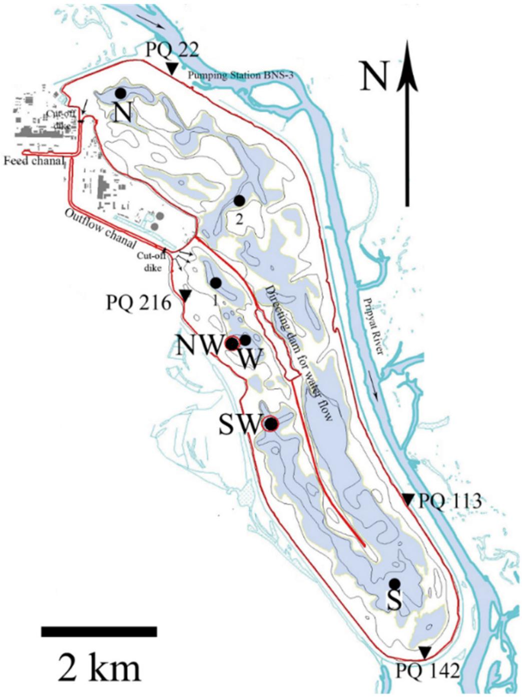

Fig. 1. Sampling locations

The ^{129}I/^{127}I ratios were obtained in the range of $(1{-}5)\times10^{-7}$. These values are two orders of magnitude higher than that of general environmental water (10^{-9}). The depth distribution of ^{129}I concentration in the water column became higher at deeper layers of the pond (Fig. 2). In fact, ^{129}I concentrations in the pore

---

[1] Ukrainian Hydrometeorological Institute

water of the bottom sediments were one order of magnitude higher than those in the pond water, indicating that radioactive iodine may be being supplied to the pond water from the sediments.

The pyrohydrolysis method was applied to three iodine species, i.e., I^-, IO_3^-, and organic-I, to investigate a suitable method for total iodine determination, and their recoveries were 87.2±7.0, 82.8±4 and 135±14.3%, respectively. Considering the composition of iodine species in environmental water, the recoveries and variations obtained in this study are unacceptable. Further studies are needed to find an appropriate method for bulk iodine measurements. We must also synthesize the organic iodine using ^{125}I as a tracer since there is no organic iodine standard that satisfies the accuracy of iodine concentration measurements by ICP-MS, whereby it is possible to confirm the recovery rates of organic iodine in water samples.

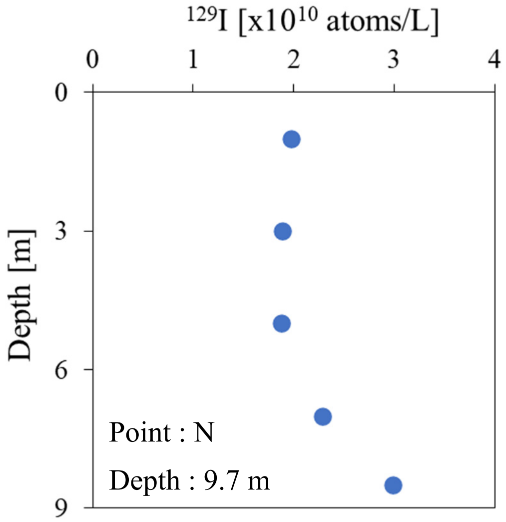

Fig. 2. Depth profile of ^{129}I (atoms/L) at point N

Reference

[1] IAEA-TECDOC-1886, IAEA Vienna (2019) P28.

3.3 Surface distribution of iodine-129 in the Okhotsk Sea

T. Matsunaka[1], S. Nagao[1], M. Inoue[1], Y. Taniuchi[2], H. Kasai[2], T. Takahashi, M. Matsumura, K. Sueki, K. Sasa

The investigation of water dynamics change in the East Asian marginal seas such as the Sea of Japan and Okhotsk Sea caused by the recent global warming is essential for forecasting the response of ocean circulation with climate change. Anthropogenic ^{129}I ($T_{1/2}$ = 15.7 million years) produced from the thermal neutron fission, is dominated by release from nuclear fuel reprocessing plants in the Europe and supplied at the Okhotsk Sea via atmospheric deposition and surface runoff. To illuminate the availability of ^{129}I as a tracer of surface circulation in the Okhotsk Sea, we investigated the horizontal distribution of ^{129}I in 2018.

The dissolved ^{129}I in surface water in the Okhotsk Sea varied from 15.0±0.7 to 26.6±0.8 nBq L^{-1}, and was negatively correlated with water temperature (Fig. 1B, $R^2 = 0.67$) and salinity (Fig. 1C, $R^2 = 0.68$). This water temperature and salinity-dependent distributions revealed that the dissolved ^{129}I in the area was controlled by mixing of water mass from the Okhotsk Sea surface seawater with cold and lower salinity and the Soya warm current from the Sea of Japan with warm and higher salinity. ^{129}I is considered to be a tracer for the front of the Okhotsk Sea surface water.

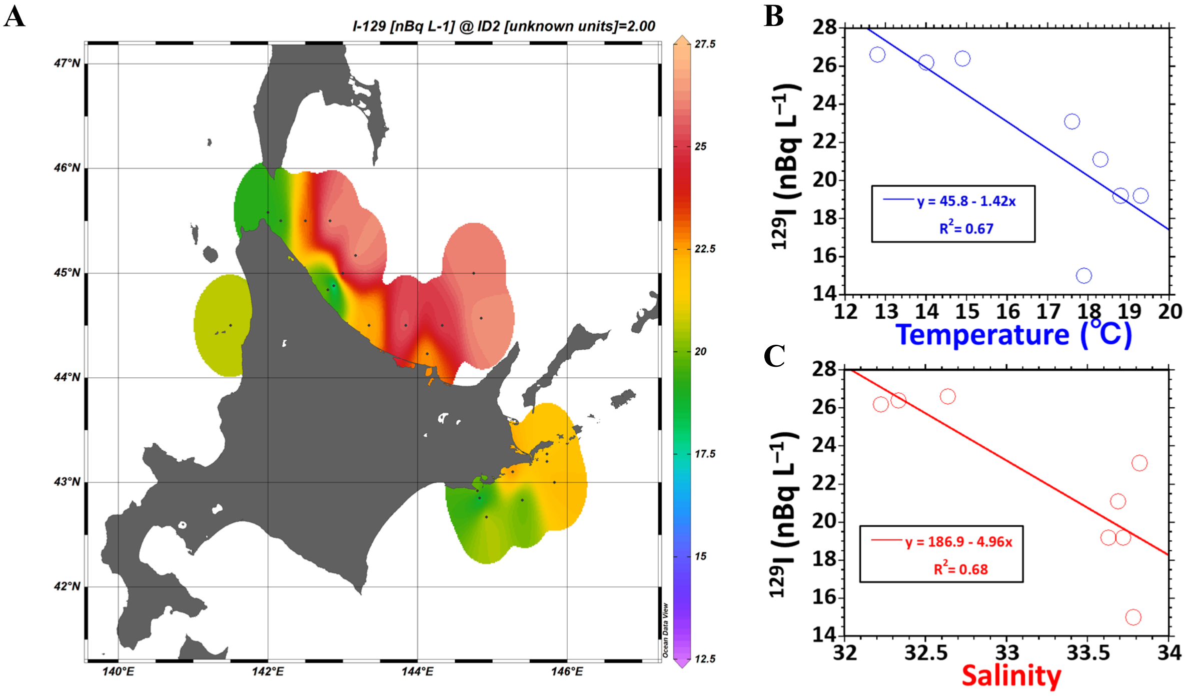

Fig. 1. Surface distribution of ^{129}I in the southern Okhotsk Sea in 2018 (A). The correlations between ^{129}I activities in surface seawater and water temperature (B) and salinity (C). The linear regression lines and coefficients of determination (R^2) are shown in the correlation diagrams.

---

[1] Kanazawa University
[2] Japan Fisheries Research and Education Agency

3.4 The Performance of Iodine-129 AMS measurements at the University of Tsukuba (FY 2020)

M. Matsumura, K. Sasa, T. Takahashi, A. Sakaguchi, T. Matsunaka[1], K. Sueki

Continuing from 2017, we have reported that the performance of ^{129}I measurement by accelerator mass spectrometry (AMS) for the development of the standard reference materials (STD) of ^{129}I in the near future. Details of the ^{129}I AMS measurements are described in the references [1-3].

From April 2020 to March 2021, we measured 257 samples of ^{129}I, the details of which are shown in Fig. 1. The test samples were chosen from natural environment such as sea, rain, river water, and soil. Figure 2 shows the measured values of carrier-reagent blanks. The machine background is estimated to be on the order of 10^{-15} in the ^{129}I/^{127}I ratio, which is sufficiently lower than the background level of the ratio of 2 × 10^{-14} for ”Old Iodine” provided from Deep Water company, USA. However, sometimes, the measured ^{129}I/^{127}I values in blanks ranged over ten times higher than 2 × 10^{-14}. One of the causes for this might be the memory effect. The rise in blank values in 2018 and 2019 is most likely caused by this memory effect, however, the memory effect has been prevented by measurement schemes since 2020.

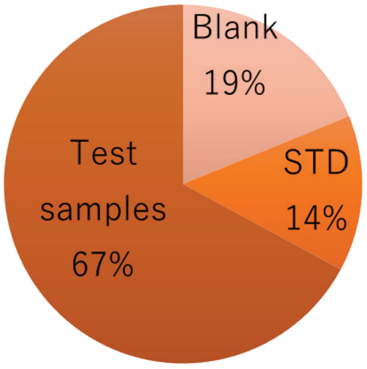

Fig. 1. Details of measured ^{129}I by the AMS system in fiscal 2020.

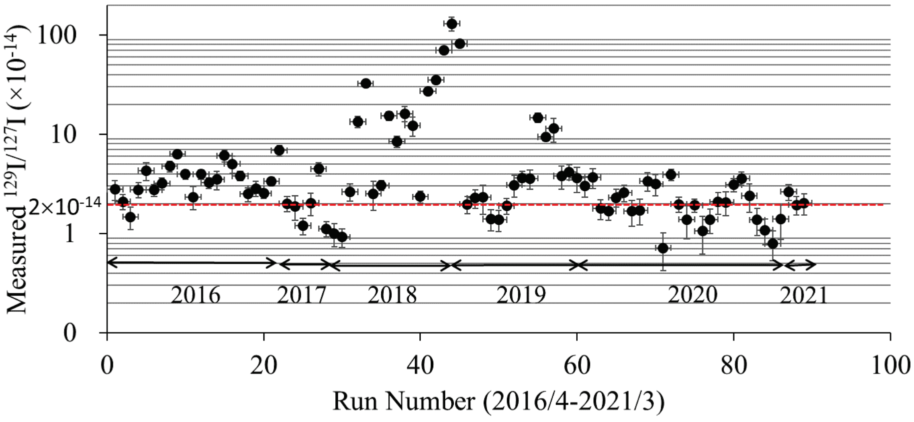

Fig. 2. ^{129}I/^{127}I ratios in blanks.

In FY 2020, we have measured the certified materials. The results of measurement for Standard Reference Material 3230, Level I and Level II, provided from the National Institute of Standards and Technology (NIST, USA) are shown in Fig. 3. They were normalized by using Purdue-2 STD (Z94-0596) with an ^{129}I/^{127}I ratio of 6.54 × 10^{-11} [4] (the value was revised in 2014 [5]), which was provided by the Purdue Rare Isotope Measurement Laboratory (PRIME Lab) at Purdue University, USA. The nominal ^{129}I/^{127}I ratios are $(4.920 \pm 0.062) \times 10^{-10}$ and $(0.985 \pm 0.012) \times 10^{-12}$, for NIST 3230- Level I and Level II, respectively. The two samples after sputter-cleaning for 1 or 5 min. were measured in each run. The measured values of Level I are 10% lower than the nominal one. The resulting ratio and standard deviation (1σ) of the precision are $(4.361 \pm 0.058) \times 10^{-10}$ (1.3%) and $(0.909 \pm 0.065) \times 10^{-12}$ (7.1%), respectively.

This work was supported in part by JSPS KAKENHI Grant Number 20H01173.

---

[1] Kanazawa University

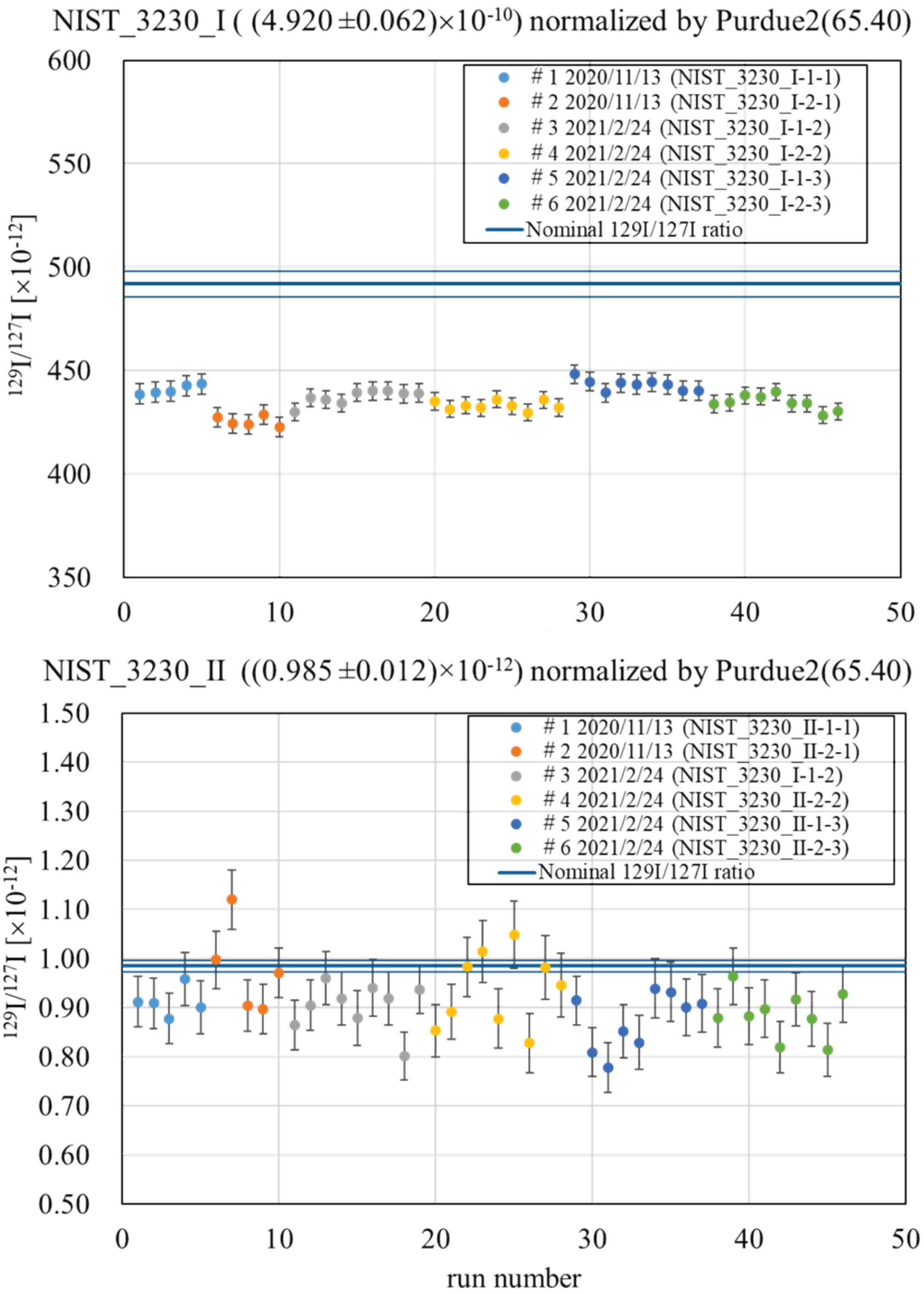

Fig. 3. Measured ^{129}I/^{127}I ratios of NIST 3230-STD. The error bars attached to measured points represent counting statistics.

References

[1] K. Sasa et al., Nucl. Instr. Meth. Phys. Res. B 437 (2018) 98.

[2] M. Matsumura et al., UTTAC Annual Report 2019, UTTAC-89 (2020) 16.

[3] K. Sasa et al., UTTAC Annual Report 2020, UTTAC-90 (2021) 16.

[4] P. Sharma et al., Nucl. Instr. Meth. Phys. Res. B 123 (1997) 347.

[5] M. Caffee, (Purdue University), Private communication (2014).

3.5 Assessing of iodine-129 in the chemical sample preparation rooms for AMS

M. Matsumura, K. Sasa, T. Takahashi, A. Sakaguchi, T. Matsunaka[1], K. Sueki

The workspace used to prepare samples for accelerator mass spectrometry (AMS) tends to become gradually contaminated through the chemical treatment of samples with high ^{129}I concentrations. Such contamination may lead to overestimated ^{129}I in AMS analyses. Thus, we have continued assessing of ^{129}I in the chemical sample preparation rooms for AMS. From 2013 to 2014, environmental ^{129}I from atmosphere was continuously monitored in the sample preparation rooms in the buildings of UTTAC and CRiED (the Center for Research in Isotopes and Environmental Dynamics, University of Tsukuba) [1, 2].

From 2017 to 2021, we measured ^{129}I from atmosphere annually in the rooms C108, C209, and C304 at UTTAC, and also in the Non-RI, RI, and ICP-MS rooms at CRiED. The experimental procedure was similar to the previous case [1, 2], except that we used a different carrier reagent "Old Iodine" provided from Deep Water company, USA, with an ^{129}I/^{127}I ratio of 2×10^{-14}. As seen in Fig. 1, the stable (^{127}I) contamination rates of less than 1 [ng (nanogram) cm^{-2} day^{-1}] from the atmosphere are rather constant in all the rooms, except for the ICP-MS room during November-December 2019. Furthermore, the ^{129}I contamination rates strongly depend on the sample-preparation history of the rooms. The levels of ^{127}I and ^{129}I contamination rates and the ^{129}I/^{127}I ratio are almost the same as or less than the previous values except for the C209-room in March 2019 [1, 2].

This work was supported in part by JSPS KAKENHI Grant Numbers 20H01173.

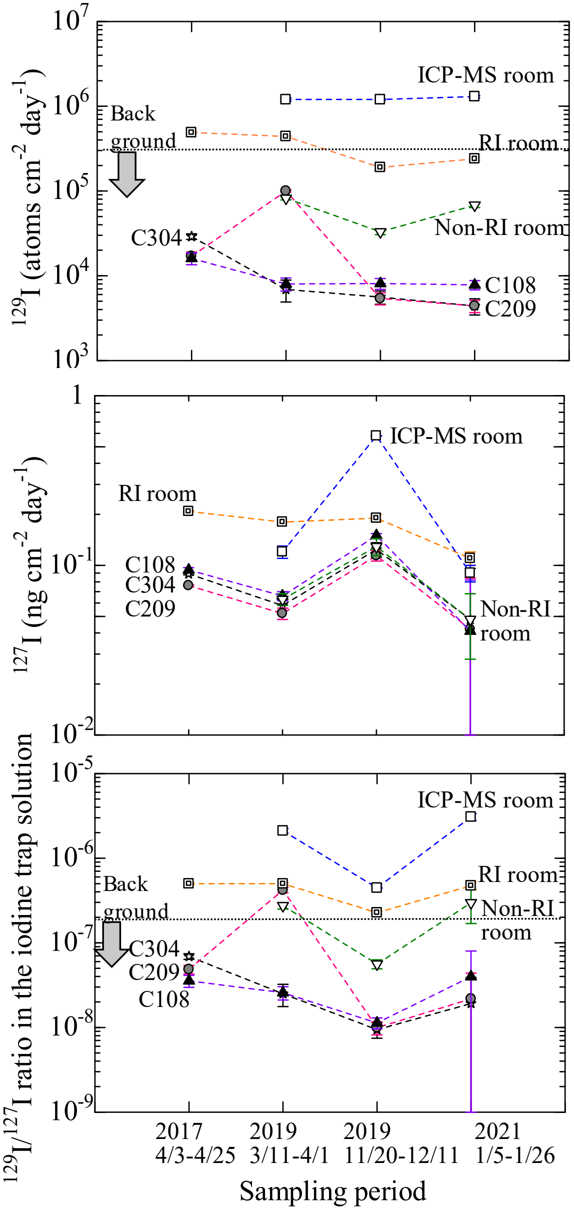

Fig. 1. Variation of the measured ^{129}I and ^{127}I contamination rates and ^{129}I/^{127}I ratio from atmosphere.

References

[1] M. Matsumura et al., UTTAC Annual Report 2014, UTTAC-84 (2015) 20.

[2] M. Matsumura et al., Anal. Sci. 36 (2020) 631. DOI: 10.2116/analsci.20SBN05

---

[1] Kanazawa University

3.6 Depth profiles of ^{129}I in soil derived from the Fukushima Dai-ichi Nuclear Power Plant

Y. Gao, A. Sakaguchi, K. Sasa, M. Matsumura, T. Takahashi, H. Yokoyama, Y. Ota, K. Sueki

A large amount of anthropogenic ^{129}I ($T_{1/2} = 1.57\times10^7$ year) was released into the environment due to the Fukushima Dai-ichi Nuclear Power Plant (FDNPP) disaster in March 2011. The anthropogenic ^{129}I of relatively single source and a short mixing time is one of the useful radioisotopes for the environmental assessment around nuclear fuel reprocessing plants. Therefore, it is important to investigate the depth distribution of radioactive ^{129}I in the environment near the FDNPP area.

In the ^{129}I studies related to the FDNPP accident, the workers have reported ^{129}I depth profiles at upland field, empty lot, and ground level in Fukushima [1]. However, their observations of change in the depth distribution have been limited to one sampling point for less than a year [2]. A long-term change of the ^{129}I distribution at a fixed point in the surrounding area of FDNPP remains unclear. In the present study, we investigate such relatively long-term migration behavior of ^{129}I.

To estimate the mobility of trace long-lived radionuclide ^{129}I in soil originating from the FDNPP accident, it is necessary to compare the depth profiles for different years. We have collected 30-cm-long soil cores at Namie-machi, Fukushima on June 12, 2013, and September 10, 2017 [3]. Before use for AMS, it was vacuum-freeze-dried and grinded using a mortar and pestle [3].

For the homogenized soil of 0.5 g, iodine was extracted by pyrohydrolysis with 0.5 g V_2O_5 [4]. Iodine thus obtained was purified by solvent extraction and then it was precipitated as AgI. The isotope ratio ^{129}I/^{127}I was measured by the AMS system at UTTAC. The ^{127}I concentration in the trap solvent obtained by pyrohydrolysis was measured with the inductively coupled plasma-mass spectrometer (ICP-MS, Agilent 8800). The deposition amounts of ^{129}I in the soil cores were calculated using ^{127}I concentration obtained from ICP-MS and ^{129}I/^{127}I ratio obtained from AMS.

Figure 1 shows the depth profiles of ^{129}I deposition amount in soil cores collected from Namie-machi, Fukushima on June 12, 2013, and September 10, 2017. In 2017. The deposition amount of the 0–9 cm (corresponding to 0 to ~70 kgm^{-2} mass depth) soil cores decreases sharply with increasing depth, while the deposition amount of 9–30 cm does not depend on depth. These characteristics are basically consistent with the results of soil core measurement in 2013. However, the accumulation at 0–30 cm is generally lower than that of 2013 soil core.

The background level for the deposition amount of 2013 soil cores at a depth of 9–30 cm is about 4.95 $\times10^{-4}$ mBq m^{-2}, while that for 2017 soil cores at a depth of 9–30 cm is about 2.31×10^{-4} mBq m^{-2}, as are shown by the vertical lines in Fig. 1. Even considering this difference in the background, the deposition amount of ^{129}I in the 0–30 cm surface soil shows an overall decreasing trend after 4 years. The different backgrounds may be due to the distance of tens of meters between the locations where the samples were collected.

Fig. 2 shows the fractions of the cumulative inventory above a certain depth to the total inventory as plotted for ^{129}I of 2013 and 2017 soil cores. In 2013, 82.9% of the FDNPP-derived ^{129}I was present with the top 22.7 kg m^{-2}, 98.2% of the FDNPP-derived ^{129}I was present with the top 49.5 kg m^{-2}. In 2017, 82.1% of the FDNPP-derived ^{129}I was present with the top 27.05 kg m^{-2}, 98.3% of the FDNPP-derived ^{129}I was present with the top 49.6 kg m^{-2}. This indicates that the FDNPP-derived radioiodine remains in the same penetration depth between 2013 and 2017.

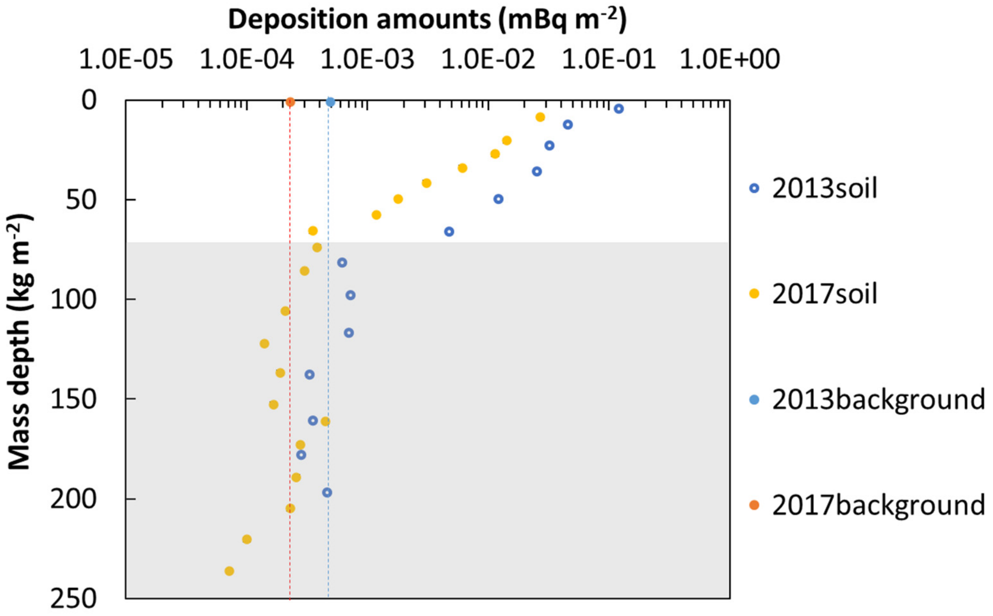

Fig. 1. Mass depth distributions of ^{129}I deposition amount in soil cores collected from Namie-machi, Fukushima on June 12, 2013, and September 10, 2017. Estimated background values are shown by the vertical dotted lines.

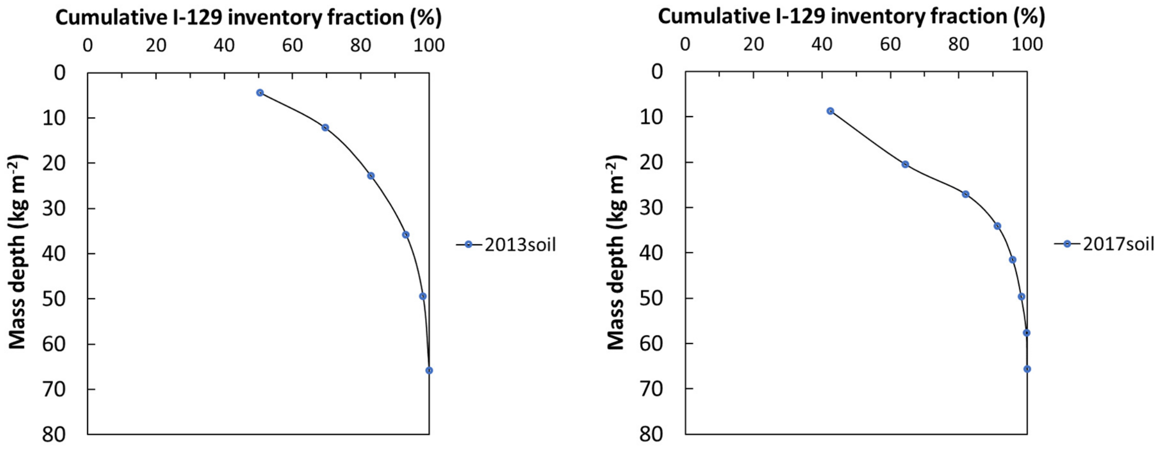

Fig. 2. The fractions of the cumulative inventory for the FDNPP ^{129}I after subtracting the ^{129}I background.

References

[1] M. Honda et al., Applied Geochem. 85 (2017) 169.
[2] M. Honda et al., J. Environ. Radioact. 146 (2015) 35.
[3] Y. Ota et al., UTTAC Annual Report 2018, UTTAC-88 (2019) 21.
[4] Y. Muramatsu et al., Quat. Geochronol. 3 (2008) 291.

4.

ION-BEAM APPLICATIONS

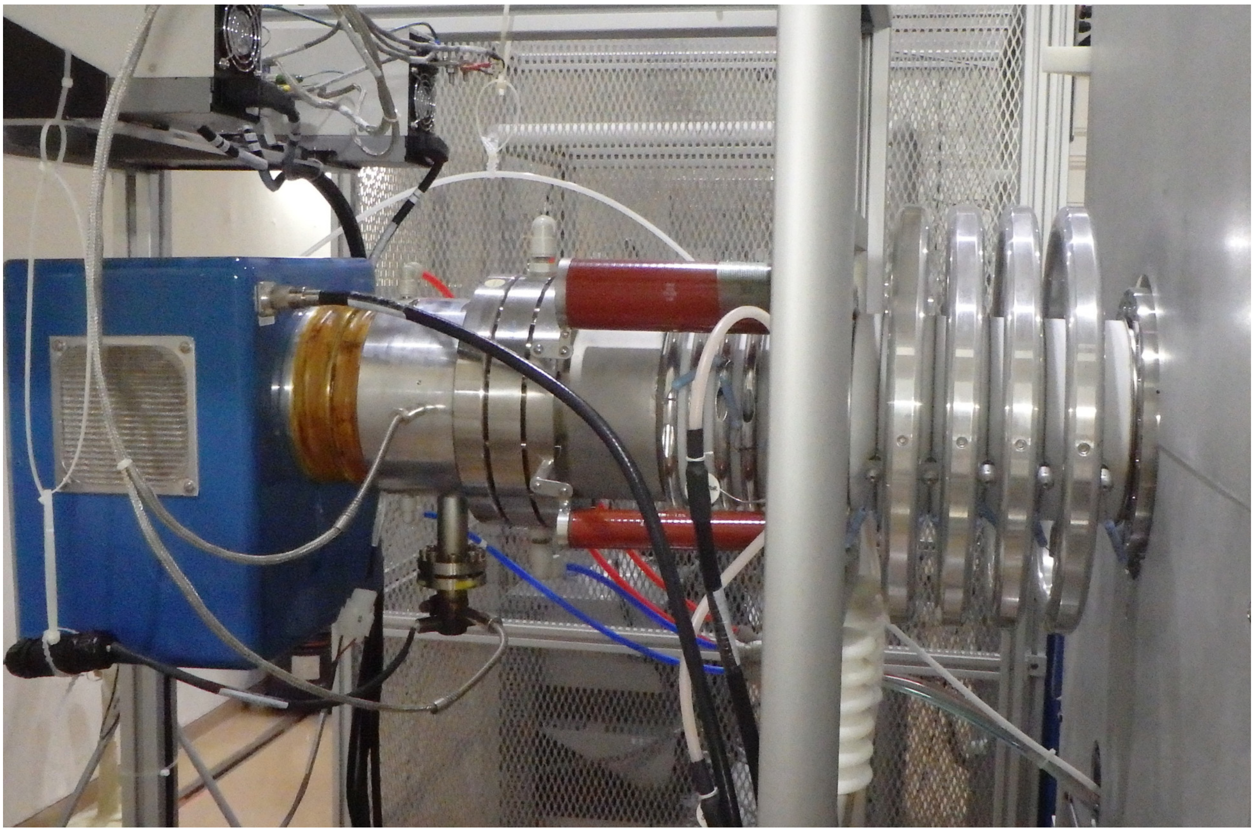

RF ion source providing a He micro-beam

4.1 In-operand lithium depth profiling by use of NRA

Y. Sugisawa, S. Kobayashi[1], N. Kishi, R. Shimizu[1, 2], T. Hitosugi[1], D. Sekiba

All-solid-state Li-ion batteries are expected as those in the next generation, which can be applied to various industrial products. Several solid electrolytes with high performance have been reported [1]. However, they still have some problems to be solved for practical applications [2]. In-situ observation of Li-ion migration during the battery operation is required to solve such problems. Nuclear reaction analysis (NRA) using $^{7}\mathrm{Li}(p, \alpha)^{4}\mathrm{He}$ is one of the direct methods for quantitative depth profiling of lithium and/or Li-ion in solid materials [3, 4]. This technique can also reduce the radiation damage of samples due to the lower energy deposition of a beam of protons than that of relatively heavier ions used for elastic recoil detection analysis (ERDA). These features of NRA are suitable for operand Li depth profiling over the whole battery stack in a single measurement. In our present study, we observed a test stack similar to the practical one under the charging and discharging conditions. We confirmed that our NRA system can visualize the transportation of Li in the sample. Furthermore, we determined the upper limit of the beam current, which does not induce dielectric breakdown of the solid electrolyte.

NRA and Rutherford backscattering spectrometry (RBS) were performed using 1 MV Tandetron at UTTAC. In the experiment, a 1.5 MeV $^{1}H^{+}$ ion beam was incident on the sample at an angle of $\theta_p = 40^\circ$ with respect to the surface normal, as shown in Fig. 1(a). The emitted α particles and backscattered H ions were detected by a solid-state detector at an angle of $\theta_e = 150^\circ$. The beam size of 1×1 mm^2 was shaped with a slit system. Figure 1(b) shows the schematic of the sample. The sample consists of a stacked layer of Li (1 μm)/Li_3PO_4 (1 μm)/Au (100 nm) deposited on a Si_3N_4 substrate of 100 nm thickness. The incident beam enters the backside of the sample to observe the Au/Li_3PO_4 (solid electrolyte) interface with a better depth resolution. Since dielectric breakdown of the electrolyte occurred for the beam current greater than 50 nA, we maintained the beam current less than 30 nA during the measurements. In this study, three measurements were performed: after charging, discharging, and recharging in the sample by changing the potential of the Au layer relative to the Li layer. We applied the potential voltage of +5 V for charging and to +0.1 V for discharging. The voltage was held during each measurement. It is expected that some fraction of Li is transported from the Li (negative electrode) layer to the Au layer in the discharging process, and reverse transportation occurs in the charging process. In addition, we note that an unexpected formation of Au-Li alloy in the Au layer is observed in the discharging process.

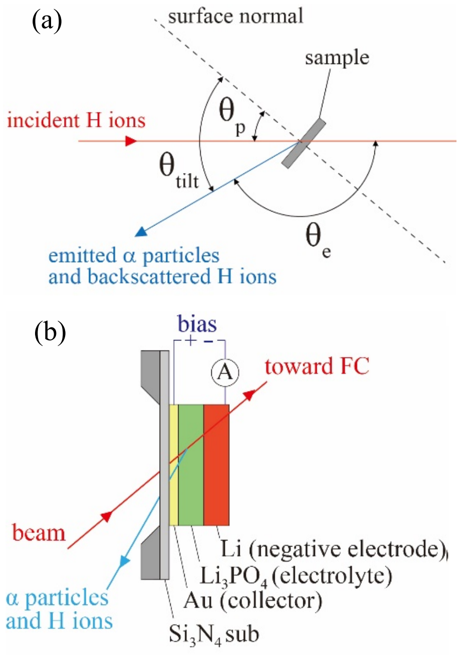

Fig. 1. Schematics of (a) the experimental arrangement and (b) the sample.

---

[1] Tokyo Inst. Tech.
[2] JST PRESTO

Figure 2 shows the energy spectra of RBS and NRA. Because of the high energy (~8 MeV) of the α particles emitted in the $^{7}Li(p, \alpha)^{4}He$ reaction, we can observe both the RBS and NRA spectra separately. The spectra obtained under the charging with +5 V (1), discharging with +0.1 V, and recharging with +5 V (2) conditions are shown by the blue, red, and green lines, respectively. The inset of Fig. 2 shows the NRA spectra which consist of three energy ranges corresponding to the Li, Li_3PO_4, and Au layers, as indicated by the broken lines. Comparison of the NRA spectra obtained at +5 V (1) and +0.1 V signifies the Li transportation from the Li layer to the Au layer. Subsequently, the Li concentrations in the Li layer and Au-Li layer are not fully recovered even under the condition at +5 V (2) for the recharging process. This result implies that significant amounts of Li ions diffuse into the Au layer and remain stable, thereby forming the Au-Li alloy.

In the RBS spectra, the assignment of each feature or contour to each element is given in Fig. 2. The spectra essentially unchanged during the charging/discharging process, except that the Au peak became wider and lower after discharging. This change also supports the stable formation of Au-Li alloy, as mentioned above. The amounts of charge transfer through the sample during discharging and recharging was 28.8 and −17.3 mC, respectively. This reduction of charge transfer agrees with the result of NRA and RBS qualitatively. The difference might be interpreted in terms of the remaining Li ion in the Au layer.

In conclusion, we confirmed that the NRA system allows measurements under operation of the all-solid-states Li-ion battery and visualize the Li transportation during the charging/discharging process. In near future, we investigate the cross-section of $^{7}Li(p, \alpha)^{4}He$ reaction in detail by ourselves. Then we will make quantitative discussion on the results obtained in the present work.

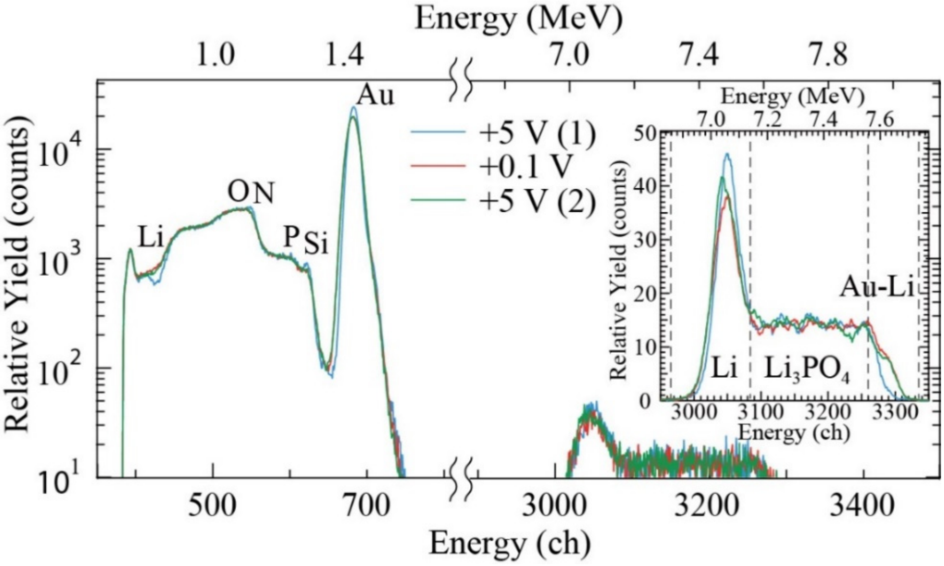

Fig. 2. RBS and NRA spectra measured for the $Li/Li_3PO_4/Au$ stack fabricated on a thin Si_3N_4 substrate.

References

[1] Y. Sun et al., Chem. Mater. 29 (2017) 5858.

[2] T. Minato, T. Abe, Progress in Surface Science 92 (2017) 240.

[3] A. Sagara et al., Nucl. Instr. Meth. Phys. Res. B 34 (1988) 465.

[4] J. Raisanen, Nucl. Instr. Meth. Phys. Res. B 66 (1992) 107.

4.2 Scanning microbeam PIXE analysis of silica glass particles released from the FDNPP

K. Sueki, T. Nakamura, S. Ishii, K. Sasa, S. Tomita, M. Sataka, H. Naramoto, H. Kudo

Due to the Fukushima Daiichi Nuclear Power Station (FDNPS) accident in March 2011, a large amount of radioactive substances was released into the environment. Among the released substances, there are particles of smaller than 1 mm diameter, called radioactive particles. It is known that radioactive particles are glassy, insoluble in water, and contain radioactive cesium as a radiation source [1]. Radioactive particles are roughly classified into two types, Type A and Type B, according to their size and the ^{134}Cs/^{137}Cs activity ratios before nuclear decay, i.e., the corrected ratios back to March 11, 2011 [1]. Type A particles derived from Units 2 or 3 of FDNPS are spherical with a diameter of about 1–10 μm, having very high specific activity and the ^{134}Cs/^{137}Cs activity ratios of about 1.0–1.1. On the other hand, Type B particles derived from Unit 1 are of an amorphous shape with a diameter of 10 μm–1 mm, having the ^{134}Cs/^{137}Cs activity ratios of about 0.93 and specific activity smaller than that of Type A particles. In previous studies, Cs L-X rays can be observed in Type A particles by scanning electron microscope (SEM/EDS) analysis equipped with an energy dispersive X-ray analyzer, and distribution information of Cs in the particles has been obtained. On the other hand, Type B particles do not contain Cs with a sufficient concentration observable by SEM/EDS analysis, hence detailed distribution information in the particles is hard to obtain.

PIXE is useful to measure heavy elements that cannot be observed by SEM/EDS. In a previous work, heavy elements (Zn, Sr, Zr, Ba and Pb) in radioactive particles were observed by PIXE using 1MV Tandetron [2]. In the present study, in order to obtain information on the element distribution in Type B particles we have applied particle induced X-ray emission method (PIXE) using the microbeam course of the 6 MV tandem accelerator at the University of Tsukuba.

The samples were irradiated with a 4 MeV proton beam focused to a size of 3–4 μm square, and the generated characteristic X-rays were measured by a cadmium telluride (CdTe) detector. The CdTe detector allowed to measure KX-rays of the elements of interest due to the relatively high detection efficiency of X-rays from 5 keV up to 100 keV, and to obtain information on the element distribution in the radioactive particles. The standard glass (NIST SRM1412a) was irradiated with a 4 MeV proton microbeam focused to a size of 4 μm square, and the generated characteristic X-rays were used for the energy calibration and the sensitivity evaluation. The X-ray sensitivity was sufficient for Zn (3.10 wt%) and Sr (3.42 wt%), but was almost at the detection limit for Ba (0.102 wt%).

Figure 1 shows the results of PEXE spectra for the two radioactive particles (particles T47 and R008) actually released in the FDNPS accident. In the spectra, we see Sr, Zr, Ba K-X rays and Pb L-X rays that could not be detected by SEM / EDS analysis. However, it is found that the target Cs spectrum is below the detection limit in terms of the detection efficiency of the CdTe detector. Figures 2 and 3 show elemental mapping for particle T47 in the area of 400 μm square and for particle R008 in the area of 250 μm square, respectively. Elemental mapping of Sr and Pb could be obtained for both particles, while for Ba the S/N ratio was too low to obtain elemental mapping. It is found from the mapping that the heavy elements of Sr and Pb are relatively uniformly distributed in the particles.

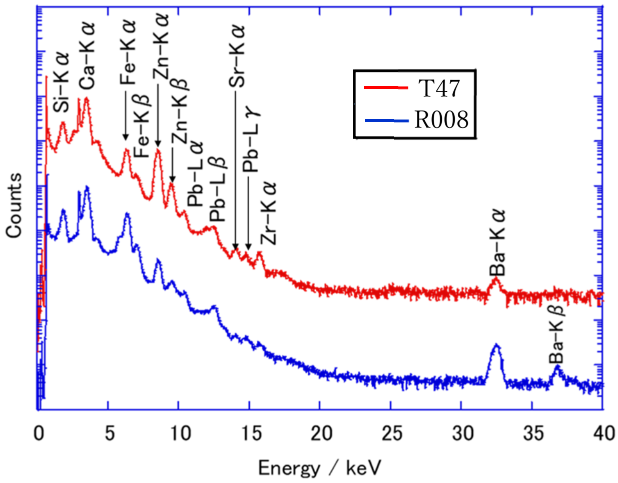

Fig. 1. PIXE spectra of radioactive particles.

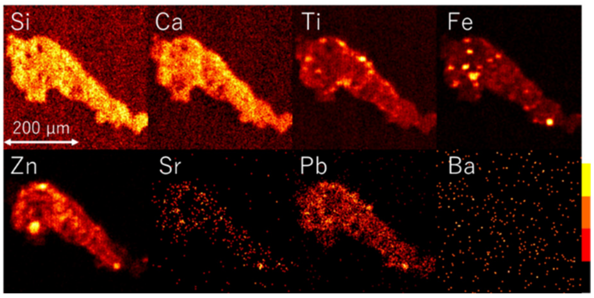

Fig. 2. PIXE images of particle T47.

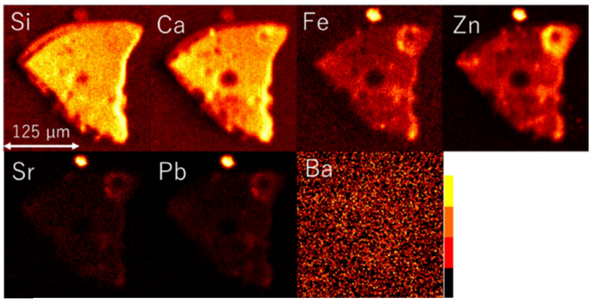

Fig. 3. PIXE images of particle R008.

References

[1] Y. Satou et al., Geochem. J. 52 (2018) 137.

[2] M. Kurosawa et al., UTTAC Annual Report 2018, UTTAC-88 (2019) 31.

4.3 Depth resolution of transmission ERDA with 8 MeV He for observation of H in solids

H. Kudo, H. Naramoto, M. Sataka, S. Ishii, K. Sasa, S. Tomita

Refinement of elastic recoil detection analysis with transmission layout (T-ERDA) is required to obtain detailed knowledge about the state or behavior of hydrogen in matter [1]. For this purpose, depth resolution of hydrogen analysis by T-ERDA has been studied by an experimental approach extended from the previously reported work [2]. As a result, we have identified the main factor determining the depth resolution of T-ERDA [3, 4].

In the present experiments, Al foils and PPS [polyphenylene sulfide $(C_6H_4S)_n$] films were stacked and used for test samples. The thicknesses of the Al foils are 5, 10, 15, 20, 50, 65, 70, 75 and 80 μm, and the PPS thickness is 1.35±0.05 μm, which is thin enough to use as an H marker. The sample names and structures are summarized in Table 1. The experimental setup and procedure are similar to the previous case [1]. A Si surface-barrier particle detector for energy analysis of H was set on the ion-beam axis and a sample was placed in front of the detector. The target-detector distance was 14 mm. The angular range of acceptance of the detector, being expressed as 0 to ϕ_m polar angle with respect to the beam axis, was adjusted by attaching a circular aperture in front of the detector. In the present experiments, we have chosen $\phi_m = 4.1°$ for narrow and 11.1° for wide tacceptance conditions, respectively. These are typical conditions chosen to obtain sufficient count rate of recoil H for a wide range of H concentration.

Table 1. Names and structures of samples for T-ERDA

Sample name	Structure
S-1	PPS on Al(50 μm)
S-2	Al(10 μm) on PPS on Al(50 μm)
S-3	Al(20 μm) on PPS on Al(50 μm)
S-4	PPS on Al(80 μm)
S-5	Al(5 μm) on PPS on Al(75 μm)
S-6	Al(10 μm) on PPS on Al(70 μm)
S-7	Al(15 μm) on PPS on Al(65 μm)

Figure 1 shows energy spectra of H measured under the narrow acceptance conditions ($\phi_m = 4.1°$) for S-1 to S-3 samples. For convenience of analysis, the yields have been scaled to have the same peak height as of S-1. We see sharp peaks originating from H in the PPS film. The three peaks are slightly asymmetric, which can be recognized by the larger number of plots (equally spaced with respect to H energy) on the left side than on the right side, indicating the existence of low-energy tails. The peak energies can be accounted for with the depth scales indicated in Fig. 1. For the three cases, however, we see slight shift of the peak energy to the low-energy side from the scale. Such peak shift arises from the finite thickness of the PPS film. Since for both the incident He and recoil H, the ratio of PPS to Al stopping power is 0.64, the effective thickness of PPS measured on the Al depth scale is 1.35 × 0:64 = 0:86 μm. Accordingly, we may expect the peak shift equal to the half thickness of 0.43 μm and thereby the observed peak shifts can be explained. In

Fig. 2, the dashed curve shows the calculated spectrum by TRIM code for 0-degree recoil of H starting from the surface of 50-μm thick Al. The peak energy of 4.31 MeV by TRIM coincides with the origin of the depth scale. About 60% of the experimental FWHM value of 0.130 MeV corresponds to the TRIM value of 0.081 MeV which is due to energy straggling.

Figure 2 shows energy spectra of H measured under wide acceptance conditions (ϕ_m =11.1°) for S-4 to S-7 samples, in which H yields are shown for the same number of incident He. Low-energy tails are more discernible than those in Fig. 1. We also see low-energy shift of the H peak from the depth scale, which is due to the PPS thickness. In Fig. 2, the dashed curve shows the calculated spectrum by TRIM for 0-degree recoil of H starting from the surface of 80-μm thick Al. Again, the peak energy of 3.77 MeV by TRIM coincides with the origin of the depth scale.

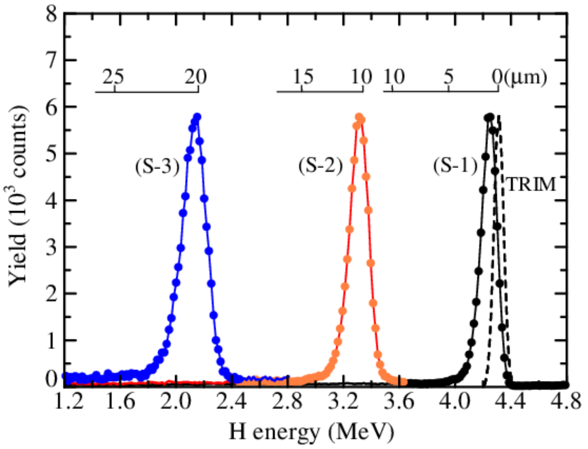

Fig. 1. T-ERDA spectra of H measured for S-1 to S-3 samples with the narrow acceptance of ϕ_m = 4.1°. The calculated spectrum using TRIM for 0-degree recoil is also shown for comparison of the peak widths.

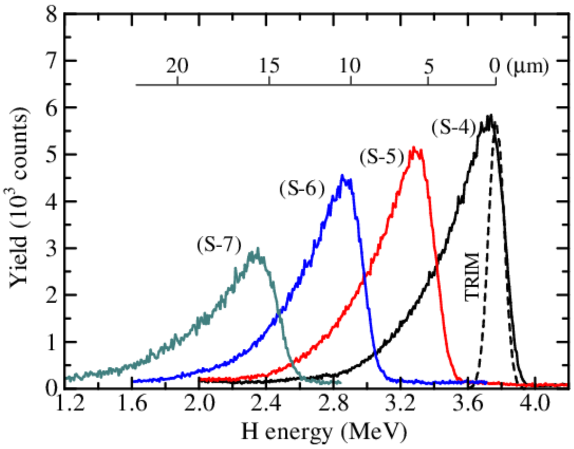

Fig. 2. T-ERDA spectra of H measured for S-4 to S-7 samples with the wide acceptance of ϕ_m = 11.1°. The calculated spectrum using TRIM for 0-degree recoil is also shown for comparison of the peak widths.

From the analysis of the experimental data, we have found that the main degrading factor for the depth resolution is the energy straggling of H in Al for narrow acceptance conditions of the detector. As the acceptance angle of the detector increases, the low-energy side of recoil H spectrum extends to form a tail, while the sharp high-energy side remains unchanged. It follows that the depth resolution is degraded by the enhanced FWHM value of the deformed triangular spectrum as a result of the extended low-energy side. However, the spectrum shape having a long tail cannot be fully characterized only by its FWHM value. The contrast of 3D image like those reported previously [1] might be more suitably understood with the sharpness of high-energy edge of the image rather than with the FWHM value. Thus, the depth resolution should be properly defined, depending on the observed image of interest.

References

[1] A. Yamazaki et al., AIP Advances 9 (2019) 105111.

[2] A. Yamazaki et al., UTTAC Annual Report 2019, UTTAC-89 (2020) 24.

[3] H. Kudo et al., arXiv:2103.13034 [physics.ins-det].

[4] H. Kudo et al., J. Phys.: Condens. Matter https://doi.org/10.1088/1361-648X/ac17ac

5.

ISOTOPE APPLICATIONS

6T superconducting magnet for Mössbauer Spectroscopy

5.1 Behaviors of vacancies in Mg-implanted GaN during ultra-high-pressure annealing studied by a monoenergetic positron beam

A. Uedono, H. Sakurai[1,2], T. Narita[3], K. Sierakowski[4], M. Bockowski[1,4], J. Suda[1], S. Ishibashi[5], S. F. Chichibu[1,6], T. Kach[1]

The GaN-based vertical power devices require embedded *p*-type regions to suppress the electric field spreading near the edges of junctions, which is effective for obtaining high breakdown voltages [1]. Ion implantation is a common technique for selective *p*-type doping, but it is well known that the removal of implantation induced defects is difficult compared with that for Si or SiC [2]. In the present study, we used a monoenergetic positron beam to study the annealing behaviors of vacancy-type defects in Mg-implanted GaN with ultra-high-pressure annealing (UHPA) process [3].

Mg^+ ions were implanted into the samples to obtain 300-nm-deep box profiles with Mg concentrations [Mg] of 1×10^{19} cm^{-3} at room temperature. The energies of Mg^+ ions were 30, 70, 150, and 300 keV, and the corresponding dosages were 2×10^{13}, 5×10^{13}, 1×10^{14}, and 3×10^{14} cm^{-2}, respectively. The samples were annealed at temperatures between 1000°C and 1480°C (5 min) under a N_2 pressure of 1 GPa using a high-nitrogen-pressure solution system.

Figure 1 shows the values of *S* parameter of Mg-implanted GaN before and after UHPA as a function of incident positron energy *E*. For the unimplanted sample, the *S* value at $E\geq20$ keV is close to *S* for defect-free GaN. For the as-implanted sample and ones annealed at 1000–1200°C, the *S* values are larger than *S* for defect-free GaN, which can be attributed to the trapping of positrons by vacancy-type defects.

The solid curves in Fig. 1 are fits to the experimental data. In the fitting, the region sampled by positrons was divided into three or four blocks. Derived depth distributions of *S* are shown in Fig. 2. Figure 3(a) and (b) shows the depth distributions of Mg and H measured by SIMS, respectively.

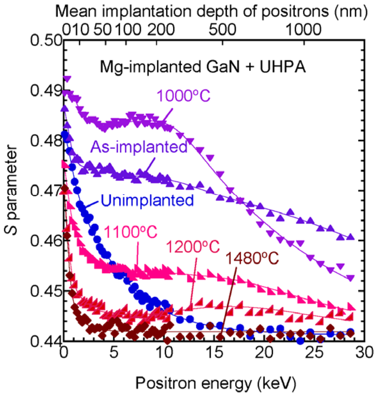

Fig. 1. *S* parameter as function of incident positron energy for Mg-implanted GaN before and after UHPA.

The incorporation of H can be attributed to unintentional moisture in the UHPA chamber. No difference in the Mg distributions for the as-implanted sample and the samples annealed at 1000–1200°C is observed. After annealing at 1300°C, Mg starts to diffuse toward the inside of the samples. The Mg distribution for the sample annealed at 1400°C is identical to that for the sample annealed at 1480°C.

---

[1] Nagoya University
[2] ULVAC Inc. Kanagawa
[3] Toyota Central R&D Labs., Inc.
[4] Polish Academy of Sciences
[5] National Institute of Advanced Industrial Science and Technology (AIST)
[6] Tohoku University

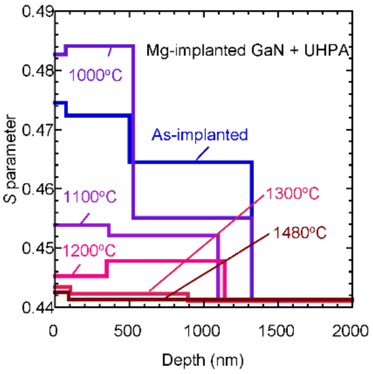

Fig. 2. Depth distributions of *S* obtained from analysis of *S*–*E* curves in Fig. 1.

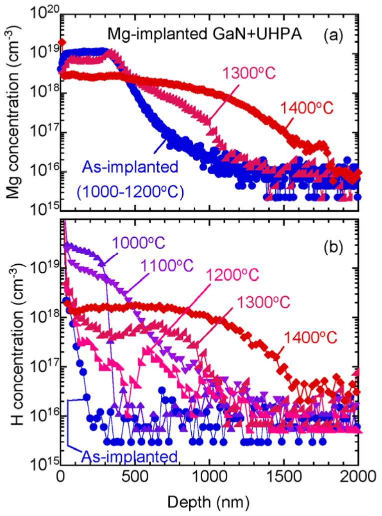

Fig. 3. Depth distributions of Mg and H for Mg-implanted GaN measured by SIMS.

In Fig. 2, for the as-implanted sample and the sample annealed at 1100°C, the position of the first and second blocks with a high *S* value (≤ 500 nm) agrees with the box profile of Mg. This can be attributed to the high [Mg] in this region and a resultant high total deposited energy of Mg that was used to substitute atoms. A damaged region was introduced up to the depth of 900–1300 nm, and this region is deeper than the block profile of Mg. This is due to the introduction of defects by Mg implanted below 300 nm and the high sensitivity of positrons to vacancy-type defects. The incorporation of H is observed after annealing at 1000°C, where the H concentration is high in the region corresponding to the Mg box profile (≤ 300 nm), and it rapidly decreases below 300 nm. The observed box profile of H is unlikely explainable assuming the diffusion model with a constant source at the surface. Thus, the major cause of the box-shape H distribution could be attributed to the trapping at vacancy-type defects. After 1100°C annealing, H atoms start to diffuse toward the bulk, and as a result, the H concentration in the subsurface region decreases. A further decrease in the H concentration is observed in the subsurface region after annealing at 1200°C. For this sample, the H concentration in the region between 500 nm and 900 nm remains high, and this region reasonably agrees with the second block (400–1100 nm) in the depth distribution of *S*. This can be attributed to the trapping of H by vacancy-type defects in the deep defect rich region and to a resultant suppression of the out-diffusion of H toward the surface. Above 1400°C annealing, both the depth distribution and the concentration of Mg almost coincide with those of H, respectively. In this temperature range, because of the decrease in the vacancy concentration (Fig. 2), the number of Mg atoms at the Ga sites increases, and as a result, the interaction between Mg_{Ga} and H is likely to enhance the incorporation of H in the sample.

References

[1] H. Amano et al., J. Phys. D: Appl. Phys. 51 (2018) 163001.

[2] S. O. Kucheyev et al., Mat. Sci. Eng. 33 (2001) 51.

[3] A. Uedono et al., Sci. Reports 10 (2020) 17349.

[4] J. L. Lyons et al., Phys. Rev. Lett. 108 (2012) 156403.

5.2 Versatile sample cooling system for Mössbauer spectroscopy using a closed-cycle refrigerator

E. Kita, S. Ishii, Y. Tajima, T. Takahashi, Y. Yamato, T. Uchida, H. Yanagihara

Temperature dependence of Mössbauer spectra generally gives us important and useful information on physical and magnetic properties of materials. In particular, for magnetic properties, magnetic transition temperature is essential physical quantity related to magnetic interaction. Additionally, Mössbauer spectroscopy (MS) is sensitive not only to a ferromagnetic order but also to an antiferromagnetic order. For low temperature measurements, we have used a bath-type cryostat, for which fixed temperature measurements at liquid nitrogen and helium are easily carried out, however, it is rather difficult to obtain an arbitrary temperature lower than ambient temperature. Closed-cycle refrigerators have been widely used for the measurement apparatuses due to the convenient utility and handling. Usual closed-cycle refrigerators generate considerable vibration resulting from mechanical motions during its operation. MS is a sensitive measurement to such vibration because its frequency is close to the energy modulation frequency. Anti-vibration refrigerators have been developed and some of them are commercially available. We used a refrigerator equipped by Iwatani Cryogenics and built up the sample cooling system.

The refrigerator includes a He condensation chamber cooled by a two-stage cooling system. A sample stage is attached outside of the He condensation chamber which is mechanically isolated from the cold head to avoid the direct transfer of vibration of cold head, as seen in Fig. 1. The sample stage is made of oxygen-free high purity copper and is finally Au-plated as seen in Fig. 2.

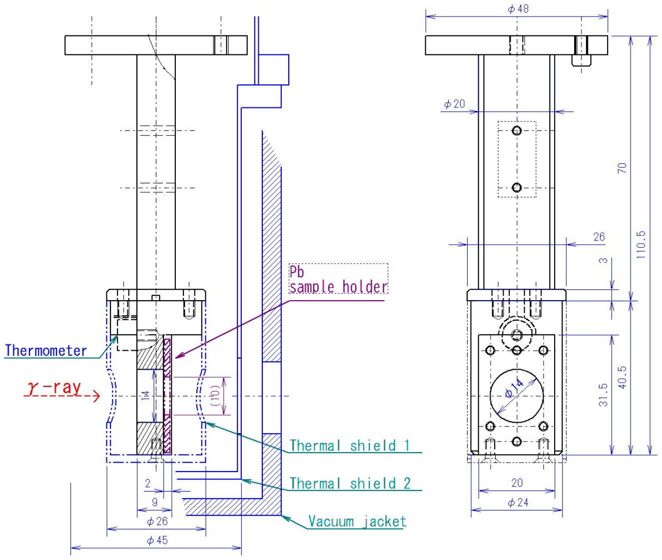

Fig. 1. Illustration of the sample stage with a Pb sample holder, two thermal shields and an outer vacuum jacket.

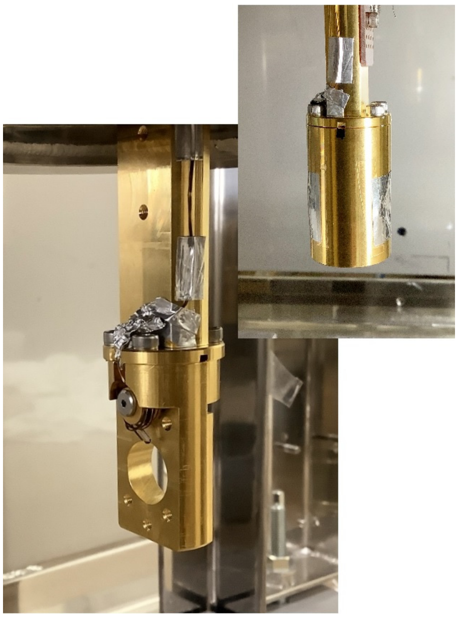

Fig. 2. Photo of the sample stage (Au plated).

To avoid heat transfer from the outside into the sample, two radiation shields were prepared. The first shield made of a Cu cylinder was set close to the sample and is depicted in Fig. 1 by the blue broken line. The 2nd one was set between the 1st shield and the outer vacuum jacket of the refrigerator. Windows for both thermal shields were covered with an Fe-free high purity Al foil with 20 μm in thickness. These radiation shields are essentially important to achieve low temperature. The lowest temperature of 2.49 K has been obtained.

Influence of vibrations caused by motions of a cold head, a compressor and an evacuation pump for a vacuum space was examined by measuring an α-Fe foil. The line width slightly increased by the operation of the cryostat system from 0.26 to 0.29 mm/s (FWHM). The sample temperature was controlled by a temperature controller, Lakeshore 335. To control remotely, a LabVIEW driver was used. An example of temperature curve during cooling is seen in Fig. 3.

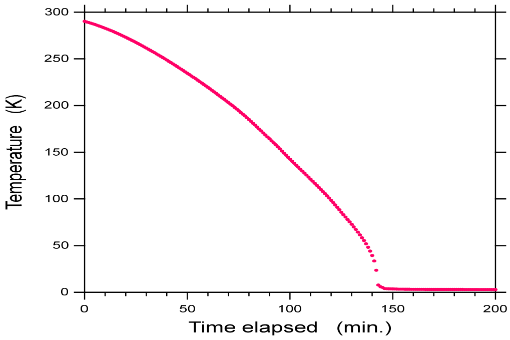

Fig. 3. Temperature vs. elapsed time

To evaluate temperature stability, we have collected MS data for FeF_2 [1]. Commercially available FeF_2 powder were used as received state. FeF_2 is known as an antiferromagnet below around 80 K. The obtained spectra are shown in Fig. 4. From the temperature dependence, clear difference is seen in the spectra between 77.526 and 78.09 K and the transition temperature is in between 78 and 80 K. Temperature fluctuation is less than 10 mK below 100 K.

We thank Prof. Mibu of Nagoya Institute of technology for the discussion on vibration. Thanks are due to Y. Takahama for his advice in operating the system and design of the sample stage and A. Yoshizumi for machining.

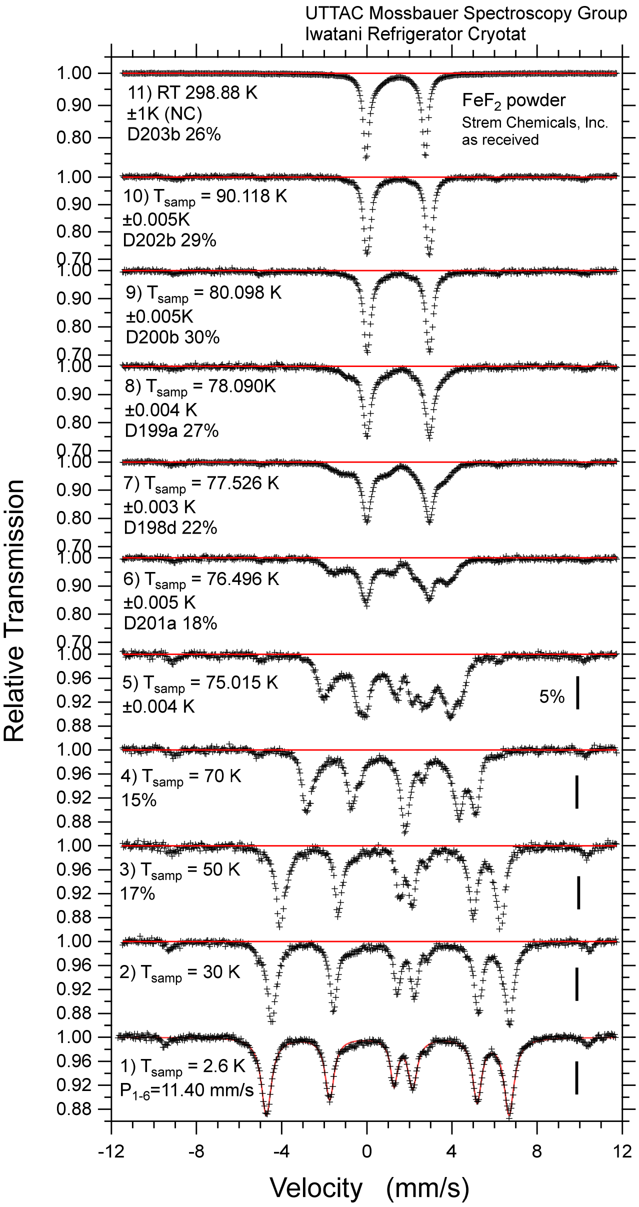

Fig. 4. Temperature dependence of Mössbauer spectra of FeF_2.

Reference

[1] G. K. Wertheim, D. N. E. Buchanan, Phys. Rev. 161 (1967) 478.

5.3 Mössbauer study of frozen magnetic fluid, Resovist

E. Kita, R. Onodera[1], M. Kishimoto, H. Yanagihara

Magnetic nanoparticles (MNPs) have been developed for novel applications in addition to their conventional applications. Recently, bio-medical application has been widely spread for such as a medical field of therapy and diagnostics, including MNP hyperthermia, drug delivery and contrast agencies for magnetic resonance imaging (MRI). The contrast agency for MRI has already been in practical use and commercially available. For these bio-medical applications, MNPs must be infused into human body, therefore MNPs are usually used in a form of magnetic fluid in which MNPs are stably suspended in solvent. Magnetic property of magnetic fluid is well described by superparamagnetism due to a time dependent magnetization behavior against an external magnetic field, so called as relaxation phenomena. Major relaxation mechanisms in the magnetic fluid are categorized in two mechanisms; one is Brown mechanism originated by the motion of magnetic particles in liquid and the other is Néel mechanism in which thermal relaxation of magnetization in a small particle is responsible. Total magnetic relaxation characterized by relaxation time of τ is composed of these two mechanisms whose characteristic times are τ_{B} and τ_{N}, i.e.,

$$\frac{1}{\tau} = \frac{1}{\tau_{\mathrm{B}}} + \frac{1}{\tau_{\mathrm{N}}} \, .$$

To understand the role of two mechanisms, separation of τ_{B} and τ_{N} is essential and usually immobilized nanoperticles have been measured to determine magnetic relaxation time, τ_{N}. Mössbauer spectroscopy (MS) has a measuring time as fast as 10^{-6} s and information on relaxation can be obtained with changing the sample temperature. For this purpose, we cooled down the MS sample to immobilize NPs instead of adding agar into the solvent. A commercially available magnetic fluid (Resovist, product of Fujifilm RI Pharma) was used for MS measurements, which was composed of a water-based suspension of carboxydextran-coated superparamagnetic iron oxide NPs.

Figure 1 shows the dimension of a liquid sample container for an MS measurement and Fig. 2 shows a

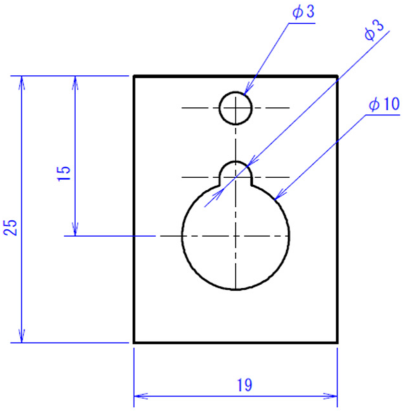

Fig. 1. Illustration of a sample container for liquid samples.

Fig. 2. Photograph of the sample container and the sample of Resovist.

---

[1] National Institute of Technology, Ibaraki College

photograph of the container made of an Al plate with a thickness of 3mm. Magnetic fluid was sealed with PET thin plates from both sides using an adhesive (Scotch Premier Gold Super Multi-Purpose Glue 2, 3M) and the sample is seen in Fig. 2.

The sample was cooled down with a closed-cycle refrigerator and the lowest temperature was 2.5 K [1]. Mössbauer spectra were recorded below the freezing point of the solvent, around 273 K.

Figure 3 shows Mössbauer spectra at different temperatures. At the lowest temperature of 2.5 K, the spectrum was fitted with Mössbauer parameters of maghemite (γ-Fe_2O_3) and the parameters are listed in Table 1. A flat base line is observed between each absorption peak suggesting that magnetic ordering without an influence of magnetic relaxation is realized. On the other hand, the spectra recorded above 100 K are influenced by the magnetic relaxation; the outer peak positions are not much moved, however, the line widths are significantly broadened. Additionally, a peak around the center grows with elevating temperature. These features are understandable by the magnetic relaxation at Fe atom. Blume-Tjon two state magnetic relaxation model [2] has been commonly used to analyze MS with relaxation and we performed fitting by using a commercially available fitting program of MossWinn4.0. The fitting taking into account of relaxation rate on the spectrum recorded at 200 K resulted in two relaxation components with relaxation times of 5.7×10^{-9} s and 1.2×10^{-7} s. These ranges of relaxation times will be useful to understand superparamagnetism of NPs together with other magnetic measurements reflecting their relaxation phenomena.

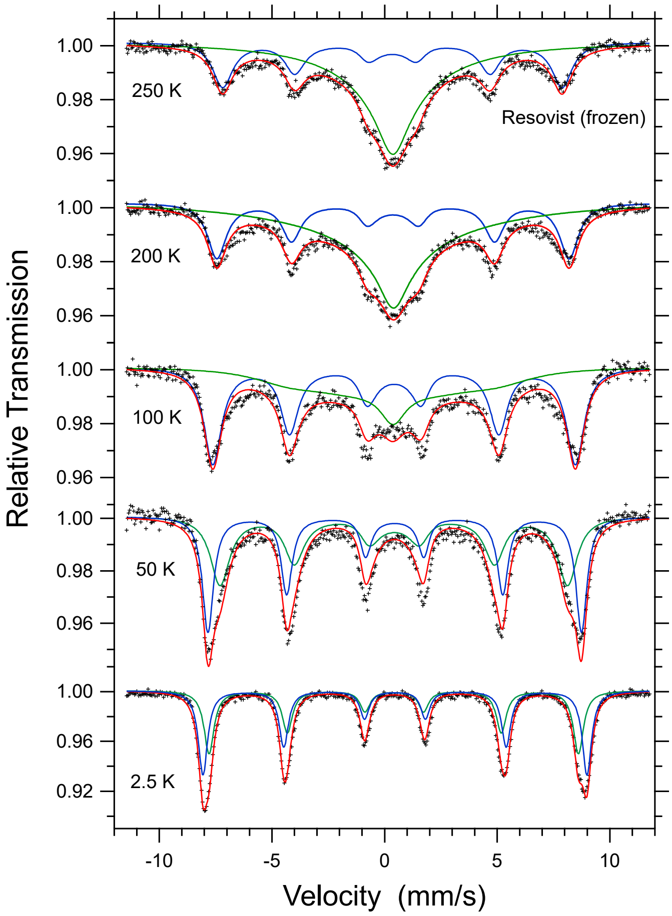

Fig. 3. Mössbauer spectra of Resovist recorded at temperatures between 2.5 K and 250 K.

Table 1. Mössbauer parameters from fitting of the spectrum recorded at 2.5K.

Site	Hhf (kOe)	IS* (mm//s)	Area ratio (%)
A	509.7	0.535	44.8
B	530.0	0.492	55.2

*IS : with respect to α-Fe at RT

References

[1] E. Kita et al., UTTAC Annual Report 2020, UTTAC-90 (2021) 34.

[2] M. Blume, J. A. Tjon, Phys. Rev. 165 (1968) 446.

5.4 Mössbauer study of Co and Mn substituted ferrite fine particles

D. Hirose, M. Kishimoto, E. Kita, H. Yanagihara

Acicular ferrite fine particles (FPs) have been developed as magnetic pigments for data storages such as magnetic recording tapes and floppy disks [1]. Additionally, the usage of fine/nano-particles has been extended to various purposes, such as bio-medical fields. For these, control of magnetic properties like saturation magnetization and anisotropy energy is still important as well as the control of size and shape of particles. Many studies have been carried out for this purpose and the effects of additional/substitutional 3d elements to ferrites on the basic magnetic properties have been well investigated. We have studied Mn and Co substitution to acicular Fe_3O_4 FPs to find a new root to produce Mn and Co ferrites FPs. Mössbauer spectroscopy was performed to understand a magnetic state of Fe atoms.

Acicular Fe_3O_4 FPs with a coercive force of 370 Oe and a saturation magnetization of 78 emu/g were used as a starting material. The starting material was dissolved in a solution of water and polyethylene glycol including substitution elements (M) ions of Co^{2+} and Mn^{2+} ions. The mixture was treated through a hydrothermal method by using an autoclave. The precipitates were washed out with water and samples were obtained by drying them at 60 °C. Nominal concentrations of substitution elements of Co and Mn were Co : Fe = 60 : 40 and Mn : Fe = 59 : 41, respectively. The dimension of products slightly increased from that of the starting material, 190 nm in length and 24 nm in diameter, through the reaction.

Mössabauer spectra were recorded with a constant acceleration mode in a velocity range of ±12 mm/s.

Table 1. Summary of M substituted Fe_3O_4, $(M)Fe_3O_4$, FP samples and Mössbauer measurements.

Sample	Element (M)	Concentration (M:Fe)	Sample ID	T_S	Measurement ID
$(Co)Fe_3O_4$	Co	60 : 40	G1H5	RT	E117
				2.6 K	D259
$(Mn)Fe_3O_4$	Mn	59 : 41	F1C1H1	RT	E118
				2.6 K	D257

Table 2. Fitting parameters for Co and Mn substituted acicular ferrite fine particles.

Sample	T_S(K)	Sub-spectrum	IS (mm/s)	QS (mm/s)	LW (mm/s)	H_{hf} (T)	Area (%)
$(Co)Fe_3O_4$	RT	Magnetic 1	0.373	–	0.387	50.9	24.7
		Magnetic 2	0.302	–	0.435	49.3	49.5
		Magnetic 3	0.532	–	0.929	45.6	25.8
	2.6	Magnetic 1	0.497	–	0.476	53.6	45.0
		Magnetic 2	0.393	–	0.442	51.2	45.7
		Magnetic 3	0.843	−0.224	1.195	47.2	9.3
$(Mn)Fe_3O_4$	RT	Magnetic 1	0.311	–	0.355	50.1	19.2
		Magnetic 2	0.286	–	0.420	48.9	38.3
		Magnetic 3*	0.582	–	(0.8)	45.5*	42.5
	2.6	Magnetic 1	0.493	−0.023	0.482	52.6	45.7
		Magnetic 2	0.425	−0.010	0.566	50.6	45.0
		Magnetic 3	0.854	−0.141	1.067	45.6	9.30

*fitted with distributed H_{hf}

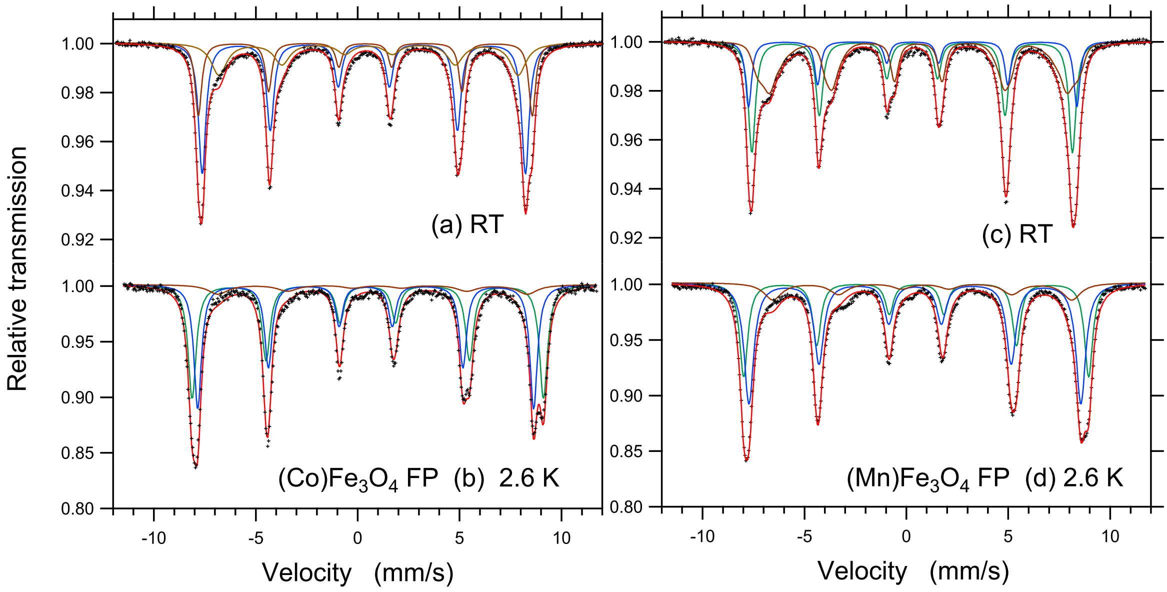

Fig. 1. Mössbauer spectra of Co substituted Fe_3O_4, (Co)Fe_3O_4, and Mn substituted Fe_3O_4, (Mn)Fe_3O_4, acicular FPs. Spectra for (Co)Fe_3O_4 FPs recorded at (a) room temperature and (b) 2.6 K are shown. Panels (c) and (d) display spectra for (Mn)Fe_3O_4 FPs recorded at room temperature and 2.6 K, respectively. Results of fitting are also displayed by solid lines for a total fitting curve (red) and sub-spectra (blue, green and brown).

Sample temperatures (T_S) were room temperature and 2.6 K. Low temperature was achieved with a refrigerator cryostat [2]. Experimental condition is listed in Table 1. Data were fitted to a combination of three magnetic sextets for all spectra at different temperatures by the use of a commercially available fitting program, MossWinn 4.0. Mössbauer parameters of isomer shift (*IS*), quadrupole splitting (*QS*), line width (*LW*) and hyperfine field (H_{hf}) were obtained for each spectrum and are summarized in Table 2.

Figure 1 shows Mössbauer spectra of Co and Mn substituted ferrite fine particles recorded at room temperature and 2.6 K. Data are plotted with black + marks and fitting results are displayed by solid lines. It is reported that Fe^{3+} ions at the spinel A site show narrow line width compared with that of B site. For Co substituted Fe_3O_4, the spectrum differs slightly from that of stoichiometric $CoFe_2O_4$. By comparing the spectrum at 2.6 K with the result in reference [3], the sub-spectrum with narrower *LW* originates from A site and one with broader *LW* from B site. The area ratios of two sites are almost equal. The spectrum for Mn substituted Fe_3O_4 recorded at RT shows high area ratio of a small H_{hf} component with a little large *IS*, which may suggest the presence of Fe^{2+} ions on B site [4]. This means that the amount of substituted Mn is not high and the sample still retains properties of Fe_3O_4.

References

[1] M. P. Sharrock, IEEE Trans. Magn. 25 (1989) 4374

[2] E. Kita et al., UTTAC Annual Report 2020, UTTAC-90 (2021) 34.

[3] R. M. Persoons et al., Phys. Rev. B 47 (1993) 5894.

[4] M. Popa et al., J. Am. Ceram. Soc. 91 (2008) 2488.

5.5 Mössbauer spectroscopy of antiferromagnetic FeMnMo alloys

F. Higashi, H. Tanimoto, E. Kita

The atomic distance in crystals increases by thermally excited lattice vibrations (thermal expansion). Due to the thermal expansion, the elastic modulus decreases with the increase in temperature. In magnetic materials, the atomic distance is normally increased along the magnetization direction (magnetostriction). When the temperature rises near the magnetic phase transition temperature, the magnetostriction becomes weaker and the atomic distance decreases with increasing temperature. Metallic materials with the temperature insensitive mechanical properties showing nearly zero thermal expansion or constant elastic modulus are known as Invar or Elinvar alloys. FeNi based alloys have been commercially used as Invar or Elinvar alloys. However, the magnetic structure of ferromagnetic alloys is sensitive to the external magnetic field and the Invar and Elinvar properties of FeNi based alloys are spoiled under magnetic field. Recently, antiferromagnetic FeMn alloys have attracted attention as new Invar or Elinvar alloys. Masumoto et al. [1, 2]. reported that FeMn alloys show the good Invar and Elinvar properties by adding 3d or 4d element. We also found that FeMnMo alloys show the good Elinvar property. In the present study, the effect of Mo addition on the antiferromagnetic property of FeMn alloys was investigated using Mössbauer spectroscopy.

FeMnMo alloy ingots with different concentrations were prepared using the arc furnace and the ingot was sliced into thin plates. The sliced plates were cold rolled and annealed, and then chemically polished. These plates of ~0.2 mm thickness, 16 mm length, and 3 mm width were used for the dynamic Young's modulus and X-ray diffraction measurements. A 5 mm square piece was cut out from the plates and thinned to about 0.02 mm by mechanical polishing with emery papers and chemical etching.

Figure 1 shows the Mössbauer spectra of the FeMnMo alloys with different compositions. For FeMn alloy system, it was reported that with the Mn content above 26% the antiferromagnetic γ-phase becomes thermally stable [3]. Quasistable ε-phase tends to be formed in FeMn alloys with the Mn content below 24% or by cold rolling. The paramagnetic and quasistable ε-phase considerably appears in the Mössbauer spectrum of Fe-25.7Mn alloy in Fig. 1. Probably, the present annealing after cold rolling was not enough for transformation of ε-phase formed by cold rolling to γ-phase. By adding a few wt% Mo to FeMn alloy, the fractional ratio of ε-phase is suppressed compared with the alloy without

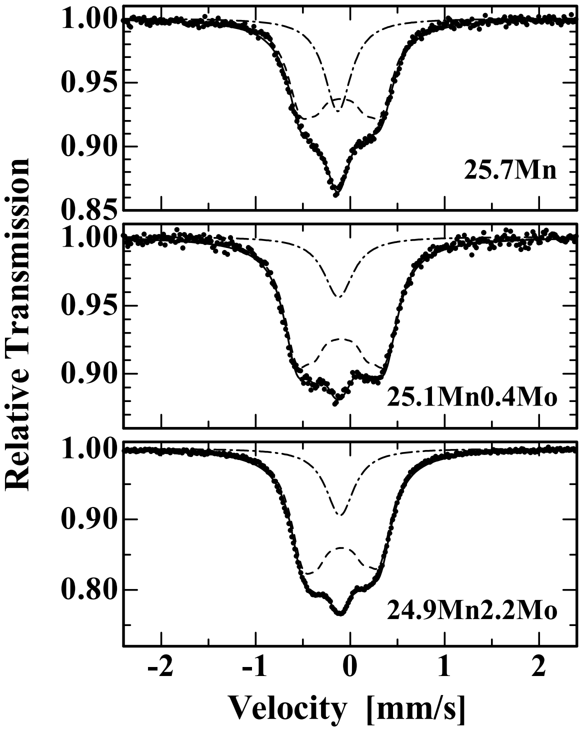

Fig. 1. Mössbaure spectra of FeMnMo alloys at room temperature. The observed data were fitted by two components of a sextet (antiferromagnetic γ-phase, broken line) and a singlet (paramagnetic ε-phase, dotted and broken lines).

Mo, suggesting that Mo also acts as the γ-phase stabilizer element like Mn. In contrast, the results of magnetization measurements revealed that the effect of Mo on the magnetic properties is opposite to that of Mn. The compositional control of Mn and Mo addition is very important for the Elinvar property at around room temperature. Toward the application to modification of Elinvar alloys, further studies on the magnetic properties as well as the texture are now in progress.

References

[1] T. Masumoto et al., Mater Trans. 58 (2017) 701

[2] K. Sugawara et al., Mater Trans. 59 (2018) 897.

[3] H. Umebayashi, Y. Ishikawa, J. Phys. Soc. Japan 21 (1966) 1281.

6.

BEAM IRRADIATION EFFECT

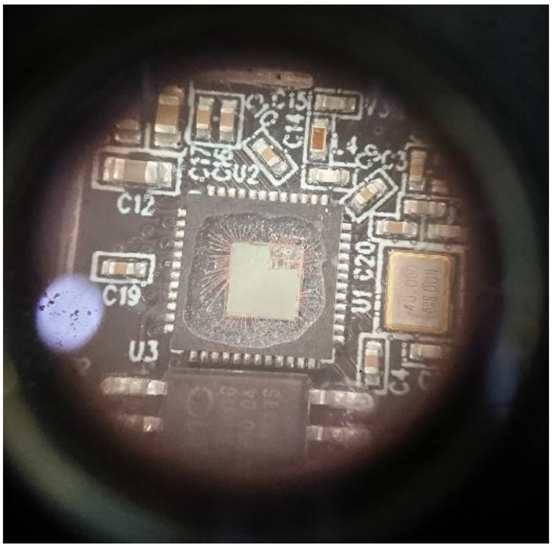

Photo by T. Okamoto

A sample of semiconductor device for radiation-tolerance test

6.1 Consumer LoRa device radiation resistance evaluation toward space application

T. Kameda, T. Okamoto

We evaluated radiation resistance of the consumer LoRa communication device, Sparkfun LoRa Gateway 1-Channel shown in Fig. 1, which is a major issue when applying this device to the special space environment of radiation exposure, and vacuum [1, 2]. The reason for selecting Sparkfun LoRa Gateway 1-Channel is that it is available in Japan at a low price and is easy to do development using the Arduino IDE. The Sparkfun LoRa Gateway 1-Channel has two semiconductor elements: the ESP32, an ultra-low power consumption IC, and the RFM95W, a 915MHz LoRa modem.

The 6MV tandem accelerator at UTTAC is equipped with L2 beam line designed for evaluation of radiation resistance. At this beamline, the Single Event Latchup (SEL) resistance of each semiconductor device was evaluated by measuring the current consumption during heavy ion irradiation shown in Table1. ESP32 was irradiated with three kinds of heavy-ion particles (Cl, F, and C), and RFM95W was irradiated with two kinds of heavy-ion particles (Cl and F).

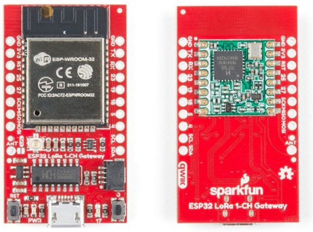

Fig. 1. Sparkfun LoRa Gateway 1-Channel

Table 1. Parameters for the evaluation test

Ion	Charge	Energy [MeV]	Range in silicon [μm]	LET [MeV/(mg/cm^2)]
Cl	7+	48	14.2	17.3
F	5+	24	14.3	7.2
C	3+	24	24.5	3.6

In ESP32, SEL occurred with Cl and F, but not with C. The relationship between the inversion cross section, obtained from the present measurements, and LET is shown in Fig. 2.

From the viewpoint of reliability engineering, the cross section was determined as if it had occurred once even when the number of SEL occurrences was zero. Because the threshold LET of ESP32 is less than 10MeV/(mg/cm^2). more detailed experiments with protons are needed for space use.

In RFM95W, no SEL occurred with all kinds of heavy ion particles, therefore RFM95W might have high resistance to SEL. Receiving probability during heavy-ion particle irradiation is shown in Figs. 3 and 4. As seen in Figs. 3 and 4, irradiation of heavy-ion particles reduces the reception rate and, accordingly, further appropriate measurements are needed.

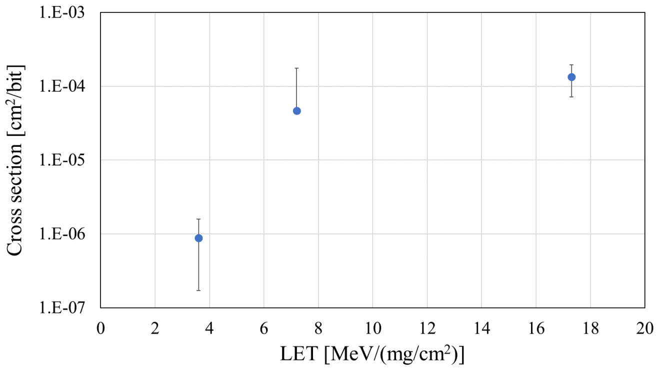

Fig. 2. SEL Cross section vs. LET

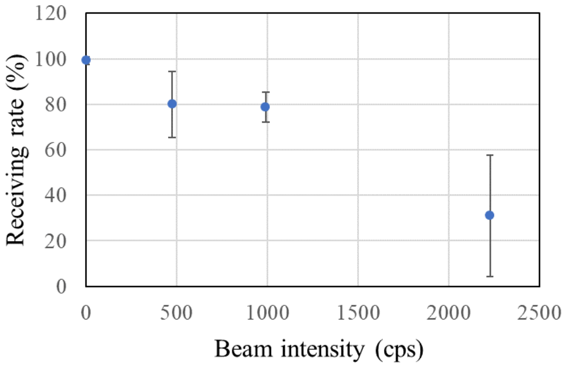

Fig. 3. Receiving rate vs. beam intensity (Cl)

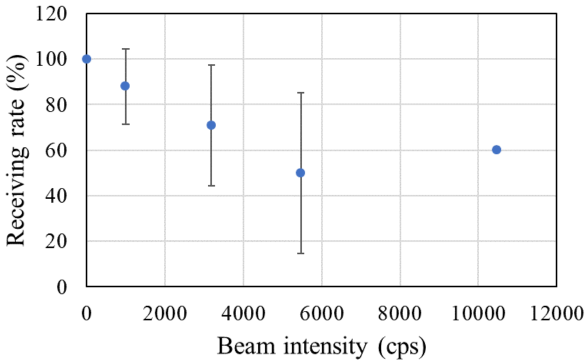

Fig. 4. Receiving rate vs. beam intensity (F)

References

[1] T. Kameda, A. Nagata, UTTAC Annual Report 2018, UTTAC-88 (2019) 47.

[2] A. Nagata et al., Trans. JSASS Aerospace Tech. Japan, Vol. 17(2) (2019) 263.

6.2 Study on microalgae mutagenesis with ^{15}N-resonant nuclear reaction

I. Suzuki, T. Yang, T. Ikeda, K. Sasa, S. Ishii, K. Tomita[1], Y. Iwata[1]

The genetic improvement through random mutagenesis, which is optimized in terms of the dose of mutagen such as effective heavy ion beams as well as typical UV-light, X-ray, gamma ray, and also such chemical agent as ethyl-methane sulfonate, is exempted from the regulation of the genetically modified organisms (GMO). There is still strong resistance in industry to the improvement through GMO to develop more desirable strains with high productivity. However, it is hard to identify the genetic mutation in terms of the dose of mutagen before selecting the mutants, much less to induce a genetic mutation expressing the target phenotypic trait in microalgae. The authors have proposed ^{15}N(^{1}H, $\alpha_1\gamma$)^{12}C resonant nuclear reaction (^{15}N-RNR) mutagenesis, which mutates the target genes of microalgae using the ^{15}N(^{1}H, $\alpha_1\gamma$)^{12}C resonant nuclear reaction [1, 2]. Nitrogen atoms commonly form chemical bonding in DNA, in which seven nitrogen atoms are contained in every pair of adenine and thymine (AT pair) and eight nitrogen atoms in every pair of guanine and cytosine (GC pair). Substituting every nitrogen atom in DNA with a stable nitrogen isotope ^{15}N enriched higher than 98% in abundance, we can obtain DNA labeled with ^{15}N isotope (^{15}N_DNA). Proton irradiation to ^{15}N_DNA induces the ^{15}N(^{1}H, $\alpha_1\gamma$)^{12}C resonant nuclear reaction at a resonant energy of 0.897 MeV, and the compound nucleus ^{16}O* subsequently produces secondary heavy ions of α (^{4}He^{2+}) and ^{12}C^{6+}, which cause high-density electronic excitation of molecules near the target ^{15}N inside ^{15}N_DNA. Resultantly, ^{15}N-specific mutagenesis to DNA is possibly realized since the density of electronic excitation by the secondary ions is 26 times higher than that of the direct electronic excitation by protons at the resonant energy. The ^{15}N-RNR mutagenesis has an advantage exceeding heavy ion irradiation of the conventional random mutagenesis, where a whole cell is exposed to high-density excitation. The 4.43 MeV gamma-rays emitted from ^{15}N(^{1}H, $\alpha_1\gamma$)^{12}C RNR are monitored from the outside of the vacuum irradiation system, which enables to accurately evaluate genetic mutation taken in ^{15}N_DNA during proton beam irradiation.

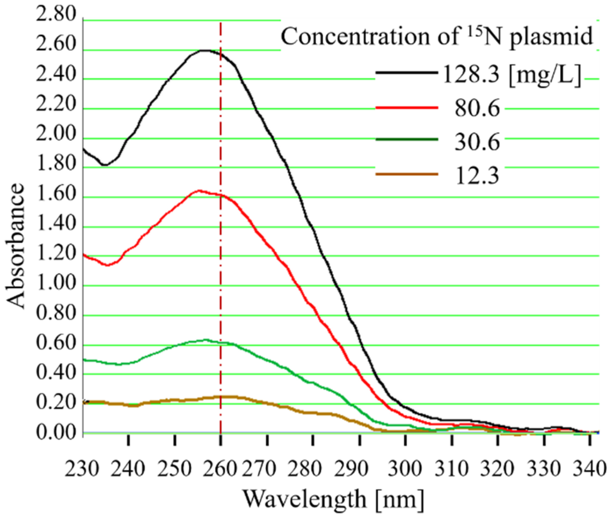

Fig. 1. Optical absorbance spectra of pUC4-KIXX plasmid DNA. 260 nm absorbance is used to quantify the concentration of nucleic acids.

The authors have demonstrated denaturation of ^{15}N_DNA induced by the ^{15}N(^{1}H, $\alpha_1\gamma$)^{12}C RNR, using UV spectrophotometry. UV spectrophotometry at 260 nm absorbance is commonly used for the quantification of nucleic acids. Figure 1 shows UV absorbance spectra of pUC4-KIXX, which is a plasmid DNA composed of 3914 bps and has two kinds of resistance genes (R-Ampicillin and R-Kanamycin). Hyperchromicity, i.e., increase in absorbance, possibly occurs by denaturation of the double-strand DNA structure separated into single

---

[1] National Institute of Advanced Industrial Science and Technology (AIST).

strands [3].

The radiation effects of proton irradiation on the ^{15}N-labeled (98% enriched) pUC4-KIXX and the natural (0.364% ^{15}N in abundance) pUC4-KIXX have been investigated by measuring 260 nm absorbance. Proton beam irradiation was carried out at energies from 0.884 to 0.906 MeV around the resonant energy of 0.897 MeV using the 1 MV Tandetron accelerator at UTTAC. The typical beam current was 1 nA in the target area of 8.3 mm^2. The 4.43 MeV gamma-rays emitted from the $^{15}N(^1H, \alpha_1\gamma)^{12}C$ RNR were detected with a BGO ($Bi_4Ge_3O_{12}$) scintillation detector.

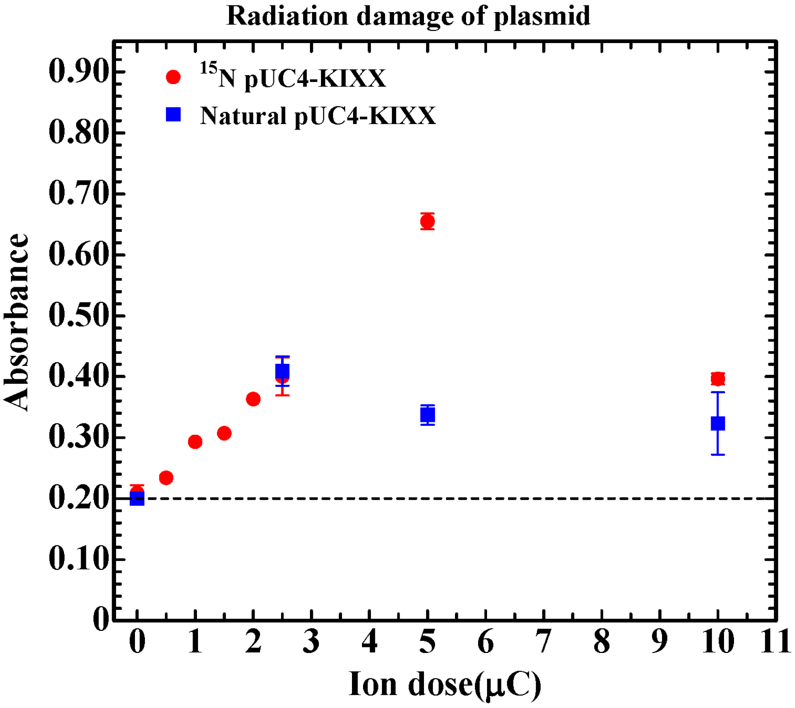

Fig. 2. Absorbance of the ^{15}N-labeled and natural pUC4-KIXX plasmids. Intense hyperchromicity of absorbance appears more significantly in the ^{15}N-labeled plasmids.

Figure 2 shows the optical absorbance of pUC4-KIXX as a function of the proton dose. Hyperchromicity is observed throughout doses from 0.5 to 10 μC. In the lower dose range, the absorbance of both the ^{15}N-labeled and natural plasmids take the same values and monotonically increase. With increasing the dose higher than 2.5 μC, the absorbance of the natural plasmid decreases, while the absorbance of the ^{15}N-labeled plasmid still increases up to 5 μC and then decreases. Intense hyperchromicity of absorbance appears more significantly in the ^{15}N-labeled plasmids, which suffer radiobiological damage by the $^{15}N(^1H, \alpha_1\gamma)^{12}C$ RNR. The denaturation of double-strand DNA into single strands is one of the possible factors of hyperchromicity, and the decrease in the absorbance indicates damage of the molecular structures of nucleic acids.

In conclusion, the authors clarified the denaturation of ^{15}N-labeled pUC4-KIXX plasmid DNA induced by the $^{15}N(^1H, \alpha_1\gamma)^{12}C$ RNR. Intense hyperchromicity in the 260 nm absorbance appears more significantly in the ^{15}N-labeled plasmid DNA.

References

[1] Y. Iwata et al., European Advanced Materials Congress (EAMC2019), Stockholm during 11–14 August (2019).

[2] Y. Iwata et al., PCT/JP2020/030476, WO/2021/029391, February 18 (2021).

[3] A. O. Nwokeoji et al., Anal. Chem. 89 (2017) 13567.

7.

LIST OF PUBLICATIONS AND PRESENTATIONS

7.1 Journals

ACCELERATOR AND RELATED FACILITIES

1. H. Matsumura, G. Yoshida, A. Toyoda, K. Masumoto, H. Nakamura, T. Miura, K. Nishikawa, K. Bessho, K. Sasa, T. Moriguchi, F. Nobuhara, Y. Nagashima, "Nondestructive High-Sensitivity Measurement Method for Activation Estimation in Accelerator Room Concrete", Radiation Protection 40(6) (2020) 677.

2. K. Masumoto, H. Matsumura, T. Miura, G. Yoshida, A. Toyoda, H. Nakamura, K. Bessho, T. Nakabayashi, F. Nobuhara, K. Sasa, T. Moriguchi, H. Tsuchida, S. Matsuyama, M. Matsuda, A. Taniike, "Evaluation of activated area in the electrostatic accelerator facilities", Radiation Protection 41(2) (2021) 145.

3. G. Yoshida, H. Matsumura, H. Nakamura, A. Toyoda, K. Masumoto, T. Miura, K. Sasa, T. Moriguchi, "Survey Methodology for the Activation of Beamline Components in an Electrostatic Proton Accelerator", Radiat. Saf. Manage. 20 (2020) 1.

NUCLEAR AND ATOMIC PHYSICS

1. Y. X. Watanabe, M. Ahmed, Y. Hirayama, M. Mukai, J. H. Park, P. Schury, Y. Kakiguchi, S. Kimura, A. Ozawa, M. Oyaizu, M. Wada, H. Miyatake, "Deexcitation γ-ray transitions from the long-lived $I^{\pi} = 13/2^{+}$ metastable state in ^{195}Os", Phys. Rev. C 101 (2020) 041305(R).

2. D. Nagae, Y. Abe, S. Okada, S. Omika, K. Wakayama, S. Hosoi, S. Suzuki, T. Moriguchi, M. Amano, D. Kamioka, Z. Ge, S. Naimi, F. Suzaki, N. Tadano, R. Igosawa, K. Inomata, H. Arakawa, K. Nishimuro, T. Fujii, T. Mitsui, Y. Yanagisawa, H. Baba, S. Michimasa, S. Ota, G. Lorusso, Yu.A. Litvinov, A. Ozawa, T. Uesaka, T. Yamaguchi, Y. Yamaguchi, M. Wakasugi, "Development and operation of an electrostatic time-of-flight detector for the Rare RI storage Ring", Nucl. Instrum. Methods Phys. Res. A 986 (2021) 164713.

3. S. Naimi, H.F. Li, Y. Abe, Y. Yamaguchi, D. Nagae, F. Suzaki, M. Wakasugi, H. Arakawa, W. Dou, D. Hamakawa, S. Hosoi, Y. Inada, K. Inomata, D. Kajiki, T. Kobayashi, M. Sakaue, K. Yokoya, T. Yamaguchi, R. Kagesawa, D. Kamioka, T. Moriguchi, M. Mukai, A. Ozawa, S. Ota, N. Kitamura, S. Masuaoka, S. Michimasa, D. S. Ahn, H. Baba, N. Fukuda, Y. Shimizu, H. Suzuki, H. Takeda, C.Y. Fu, Z. Ge, S. Suzuki, Q. Wang, M. Wang, Yu.A. Litvinov, G. Lorusso, T. Uesaka, "Experimental Challenges of the First Mass Measurement Campaign at the Rare-RI Ring", J. Phys. Conf. Ser. 1643

(2020) 012058.

4. T. Moriguchi, M. Amano, A. Ozawa, W. Horiuchi, Y. Abe, T. Fujii, R. Kagesawa, D. Kamioka, A. Kitagawa, M. Mukai, D. Nagae, M. Sakaue, S. Sato, S. Suzuki, T. Suzuki, T. Yamaguchi, K. Yokota, "Measurements of total reaction cross sections for ^{17}Ne using a solid hydrogen target", J. Phys. Conf. Ser. 1643 (2020) 012099.

5. A. Homma, M. Tanaka, M. Takechi, T. Ohtsubo, M. Fukuda, T. Suzuki, D. Nishimura, T. Moriguchi, D. S Ahn, A. S Aimaganbetov, M. Amano, H. Arakawa, S. Bagchi, K.-H. Behr, N. Burtebayev, K. Chikaato, H. Du, T. Fujii, N. Fukuda, H. Geissel, T. Hori, S. Hoshino, R. Igosawa, A. Ikeda, N. Inabe, K. Inomata, K. Itahashi, T. Izumikawa, D. Kamioka, N. Kanda, I. Kato, I. Kenzhina, Z. Korkulu, Ye. Kuk, K. Kusaka, K. Matsuta, M. Mihara, E. Miyata, D. Nagae, S. Nakamura, M. Nassurlla, K. Nishimuro, K. Nishizuka, S. Ohmika, K. Ohnishi, M. Ohtake, H.J. Ong, A. Ozawa, A. Prochazka, H. Sakurai, C. Scheidenberger, Y. Shimizu, T. Sugihara, T. Sumikama, S. Suzuki, H. Suzuki, H. Takeda, Y. Tanaka, Y. K. Tanaka, T. Wada, K. Wakayama, S. Yagi, T. Yamaguchi, R. Yanagihara, Y. Yanagisawa, K. Yoshida, T. K. Zholdybayev, "Development of a Method to Deduce Point-proton Radii from Charge Changing Cross Sections", JPS Conf. Proc. 32 (2020) 010032.

6. M. Mukai, Y. Hirayama, Y. X. Watanabe, S. Schiffmann, J. Ekman, M. Godefroid, P. Schury, Y. Kakiguchi, M. Oyaizu, M. Wada, S. C. Jeong, J. Y. Moon, J. H. Park, H. Ishiyama, S. Kimura, H. Ueno M. Ahmed, A. Ozawa, H. Watanabe, S. Kanaya, H. Miyatake, "In-gas-cell laser resonance ionization spectroscopy of ^{196,197,198}Ir", Phys. Rev. C 102 (2020) 054307.

7. C. Y. Fu, Y. H. Zhang, M. Wang, X. H. Zhou, Yu. A. Litvinov, K. Blaum, H. S. Xu, X. Xu, P. Shuai, Y. H. Lam, R. J. Chen, X. L. Yan, X. C. Chen, J. J. He, S. Kubono, M. Z. Sun, X. L. Tu, Y. M. Xing, Q. Zeng, X. Zhou, W. L. Zhan, S. Litvinov, G. Audi, T. Uesaka, T. Yamaguchi, A. Ozawa, B. H. Sun, Y. Sun, F. R. Xu, "Mass measurements for the T_z = -2 f p-shell nuclei ^{40}Ti, ^{44}Cr, ^{46}Mn, ^{48}Fe, ^{50}Co, and ^{52}Ni", Phys. Rev. C 102 (2020) 054311.

ACCELERATOR MASS SPECTROMETRY

1. Kimikazu Sasa, Maki Honda, Seiji Hosoya, Tsutomu Takahashi, Kenta Takano, Yuta Ochiai, Aya Sakaguchi, Saori Kurita, Yukihiko Satou, Keisuke Sueki, "A sensitive method for Sr-90 analysis by accelerator mass spectrometry" J. Nucl. Sci. Tech. 58(1) (2021) 72-79.
   [DOI: 10.1080/00223131.2020.1801530]

2. Masumi Matsumura, Kimikazu Sasa, Tetsuya Matsunaka, Keisuke Sueki, Tsutomu Takahashi, Hiroyuki Matsuzaki, "Assessing the effect of laboratory environment on sample contamination for

I-129 accelerator mass spectrometry", Anal. Sci. 36(5) (2020) 531. [DOI: 10.2116/ analsci.20SBN05]

BEAM AND ISOTOPE APPLICATIONS

1. M. Kurosawa, K. Sasa, S. Ishii, "Quantitative PIXE analyses of trace Ti in single fluid inclusions in quartz from Tsushima granite", Nucl. Instrum. Methods Phys. Res. B 479 (2020) 35.

2. T. Yamamoto, A. Chikamatsu, S. Kitagawa, N. Izumo, S. Yamashita, H. Takatsu, M. Ochi, T. Maruyama, M. Namba, W. Sun, T. Nakashima, F. Takeiri, K. Fujii, M. Yashima , Y. Sugisawa, M. Sano, Y. Hirose, D. Sekiba, C. M. Brown, T. Honda, K. Ikeda, T. Otomo, K. Kuroki, K. Ishida, T. Mori, K. Kimoto ,T. Hasegawa, H. Kageyama, "Strain-induced creation and switching of anion vacancy layers in perovskite oxynitrides", Nat. Commun. 11 (2020) 5923.

3. K. Hirota, G. Ichikawa, S. Ieki, T. Ino, Y. Iwashita, M. Kitaguchi, R. Kitahara, J. Koga, K. Mishima, T. Mogi, K. Morikawa, A. Morishita, N. Nagakura, H. Oide, H. Okabe, H. Otono, Y. Seki, D. Sekiba, T. Shima, H. M. Shimizu, N. Sumi, H. Sumino, T. Tomita, H. Uehara, T. Yamada, S. Yamashita, K. Yano, M. Yokohashi, T. Yoshioka, "Neutron lifetime measurement with pulsed cold neutrons", Prog. Theor. Exp. Phys. 2020 (2020) 123C02.

4. T. Wakasugi, Y. Hirose, S. Nakao, Y. Sugisawa, D. Sekiba, T. Hasegawa, "High-Quality Heteroepitaxial Growth of Thin Films of the Perovskite Oxynitride $CaTaO_2N$: Importance of Interfacial Symmetry Matching between Films and Substrates", ACS Omega 5 (2020) 1339.

5. S. Yamada, R. Shigesawa, H. Latiff, M. Kishimoto, E. Kita, H. Yanagihara, "Magnetic Properties of Tetragonal Cobalt Manganese Ferrite Particles Prepared Using the Molten Salt Method", IEEE Trans. Magn. 56(4) (2020) 6702618.

6. R. Murase, H. Tsuchida, S. Tomita, A. Chiba, K. Nakajima, T. Majima, M. Saito, "Effects of molecular axis orientation of MeV diatomic projectiles on secondary ion emission from biomolecular targets", Nucl. Instrum. Meth. Phys. Res. B 478 (2020) 284.

7. M. Sumiya, M. Sumita, Y. Asai, R. Tamura, A. Uedono, A. Yoshigoe, "Dynamic Observation and Theoretical Analysis of Initial O_2 Molecule Adsorption on Polar and *m*-Plane Surfaces of GaN", J. Phys. Chem. 124 (2020) 25282-25290. [DOI: 10.1021/acs.jpcc.0c07151]

8. A. Uedono, H. Sakurai, T. Narita, K. Sierakowski, M. Bockowski, J. Suda, S. Ishibashi, S. F. Chichibu, T. Kachi, "Effects of ultra-high-pressure annealing on characteristics of vacancies in Mg-implanted GaN studied using a monoenergetic positron beam", Sci. Rep. 10 (2020) 17349 (1-7). [DOI:

10.1038/s41598-020-74362-9]

9. F. Inoue, A. Podpod, L. Peng, A. Phommahaxay, K. J. Rebibis, A. Uedono, E. Beyne, “Morphological characterization and mechanical behavior by dicing and thinning on direct bonded Si wafer”, J. Manuf. Process. 58 (2020) 811-818. [DOI: 10.1016/j.jmapro.2020.08.050]

10. A. Uedono, K. Shojiki, K. Uesugi, S. F. Chichibu, S. Ishibashi, M. Dickmann, W. Egger, C. Hugenschmidt, H. Miyake, “Annealing behaviors of vacancy-type defects in AlN deposited by radio-frequency sputtering and metalorganic vapor phase epitaxy studied using monoenergetic positron beams”, J. Appl. Phys. 128 (2020) 085704(1-10). [DOI: 10.1063/5.0015225]

11. S. Chang, M. Zhao, V. Spampinato, A. Franquet, T.-H. Do, A. Uedono, T. T. Luong, T.-H. Wang, L. Chang, “The Influence of AlN Nucleation Layer on Radio Frequency Transmission Loss of AlN-on-Si Heterostructure”, Phys. Stat. Sol. (a) 217 (2020) 1900755(1-6). [DOI: 10.1002/pssa.201900755]

12. H. J. Zhang, S. Sellaiyan, K. Sako, A. Uedono, Y. Taniguchi, K. Hayashi, “Effect of Free-Volume Hole Fraction on Dynamic Mechanical Properties of Epoxy Resins Investigated by Pressure-Volume-Temperature Technique”, J. Phys. Chem. B 124 (2020) 1824-1832. [DOI : 10.1021/acs.jpcb.9b10978]

13. A. Uedono, W. Ueno, T. Yamada, T. Hosoi, W. Egger, T. Koschine, C. Hugenschmidt, M. Dickmann, H. Watanabe, “Voids and vacancy-type defects in SiO$_2$/GaN structures probed by monoenergetic positron beams”, J. Appl. Phys. 127 (2020) 054503(1-8). [DOI: 10.1063/1.5134513]

14. A. Sagara, H. Yabe, X. Chen, P.M. Vereecken, A. Uedono, “Pore structure analysis of ionic liquid-templated porous silica using positron annihilation lifetime spectroscopy”, Microporous Mesoporous Mat. 295 (2020) 109964(1-7). [DOI: 10.1016/j.micromeso.2019.109964]

15. N. Qi, X. Zhang, Z. Q. Chen, F. Ren, B. Zhao, M. Jiang, A. Uedono, “Selective trapping of positrons by Ag nanolayers in a V/Ag multilayer system”, AIP Adv. 10 (2020) 035012(1-7).
[DOI: 10.1063/1.5143379]

16. H. J. Zhang, S. Sellaiyan, K. Sako, A. Uedono, Y. Taniguchi, K. Hayashi, “Effect of free-volume holes on static mechanical properties of epoxy resins studied by positron annihilation and PVT experiments”, Polymer 190 (2020) 122225(1-9). [DOI: 10.1016/j.polymer.2020.122225]

17. G. A. Jacob, S. Sellaiyan, A. Uedono, R. J. Joseyphus, “Magnetic properties of metastable bcc phase in Fe$_{64}$Ni$_{36}$ alloy synthesized through polyol process”, Appl. Phys. A 126 (2020) 120(1-7).
[DOI: 10.1007/s00339-020-3292-3]

18. T. Kimura, K. Kataoka, A. Uedono, H. Amano, D. Nakamura, “Growth of high-quality GaN by halogen-free vapor phase epitaxy”, Appl. Phys. Express 13 (2020) 085509(1-5). [DOI: 10.35848/1882-0786/aba494]

19. S. F. Chichibu, A. Uedono, K. Kojima, K. Koike, M. Yano, S. Gonda, S. Ishibashi, “Hole capture-coefficient of intrinsic nonradiative recombination centers that commonly exist in bulk, epitaxial, and proton-irradiated ZnO”, Appl. Phys. Lett. 127 (2020) 215704(1-6). [DOI: 10.1063/5.0011309]

7.2 Reviews and books

1. 笹 公和，“難測定核種の加速器質量分析による高感度検出手法の開発”，応用物理学会放射線分科会会誌「放射線」45(3) (2020) 128.

2. D. Sekiba, “Nuclear Methods in Surface Science” In: Rocca M., Rahman T.S., Vattuone L. (eds) Springer Handbook of Surface Science. Springer Handbooks. Springer, Cham. https://doi.org/10.1007/978-3-030-46906-1_39

7.3 Poster or oral presentations at academic meetings

1. A. Uedono, H. Sakurai, T. Narita, K. Sierakowski, M. Bockowski, J. Suda, S. Ishibashi, S. F. Chichibu, T. Kachi, “Behaviors of vacancy-type defects in Mg-implanted GaN during ultra-high-pressure annealing studied by using a monoenergetic positron beam”, SPIE Photonics West, OPTO, San Francisco, USA (Mar. 6, 2021). (Invited Talk)

2. A. Uedono, H. Iguchi, T. Narita, K. Kataoka, W. Egger, T. Koschine, C. Hugenschmidt, M. Dickmann, K. Shima, K. Kojima, S. F. Chichibu, S. Ishibashi, “Interaction between hydrogen and vacancy-type defects in Mg-implanted GaN studied by monoenergetic positron beams”, Int. Work. Positron Study Defects, on-line (Mar. 3, 2021). (Invited Talk)

3. A. Uedono, M. Dickmann, W. Egger, C. Hugenschmidt, S. Ishibashi, “A study of vacancy-type defects in wide-gap semiconductors by means of positron annihilation spectroscopy”, MLZ User Meeting and German Neutron Scattering Conf., Germany (Dec. 8, 2020). (Invited Talk)

4. 上殿明良， 高島信也， 江戸雅晴， 上野勝典， 松山秀昭，M. Dickmann，W. Egger，C. Hugenschmidt，嶋 紘平，小島一信，秩父重英，石橋章司，“陽電子消滅法による Mg イオン注入 GaN の空孔型欠陥の焼鈍特性及び欠陥によるキャリア捕獲の研究”，先進パワー半導体分科会－応用物理学会，オンライン開催 (2020 年 11 月 16 日). （招待講演）

5. 上殿明良，櫻井秀樹，成田哲生，K. Sierakowski，M. Bockowski，須田　淳，石橋章司，嶋　紘平，秩父重英，加地　徹，“陽電子を用いた超高圧焼鈍によるイオン注入 GaN の欠陥回復特性の研究”，第 49 回結晶成長国内会議，オンライン開催 (2020 年 11 月 9 日).（招待講演）

6. A. Ozawa, “Present status of Rare-RI Ring (R3) and mass measurements”, RIBF Users Meeting 2020, RIKEN, on-line (Sep. 8-10, 2020). (Invited Talk)

7. 冨田成夫，山崎明義，石井　聡，笹 公和，左高正雄，檜本　洋，工藤　博，“透過 ERDA によるアルミニウム中の水素 3 次元計測”，第 68 回応用物理学会春季学術講演会シンポジウム「イオンビーム分析の最前線と展望」， オンライン開催　(2021 年 3 月 16-19 日).（招待講演）

8. 笹　公和，“加速器質量分析を用いた宇宙線生成核種および人為起源核種の環境動態研究”，金沢大学環日本海域環境研究センター セミナー，金沢大学 (2020 年 11 月 17 日).（招待講演）

9. A. Sakaguchi, “Accelerator mass spectrometry analyses of ultra-trace radionuclides in the environment - application to geosciences studies”, Forum for Nuclear Cooperation in Asia, (Mar. 3-4, 2021). (Invited Talk)

10. 上殿明良，正直花奈子，上杉謙次郎，秩父重英，石橋章司，M. Dickmann，W. Egger，C. Hugenschmidt，三宅秀人，”陽電子消滅によるスパッタ堆積 AlN 薄膜中の空孔型欠陥検出”，第 68 回応用物理学会春季学術講演会，オンライン開催 (2021 年 3 月 19 日).

11. 秩父重英，嶋　紘平，小島一信，B. Moody，三田清二，R. Collazo，Z. Sitar，熊谷義直，上殿明良，“AlN 単結晶上に HVPE 成長させた Si 添加 AlN 基板の発光特性”，第 68 回応用物理学会春季学術講演会，オンライン開催 (2021 年 3 月 19 日).

12. 嶋　紘平，田中　亮，高島信也，上野勝典，江戸雅晴，小島一信，上殿明良，秩父重英，“Mg イオン注入後の空孔ガイド拡散法により形成した p 型 GaN のルミネッセンス評価”，第 68 回応用物理学会春季学術講演会，オンライン開催 (2021 年 3 月 18 日).

13. 角谷正友，高原悠希，今中康貴，A. Amira，G. Andersson，竹端寛治，上殿明良，“AlN テンプレート上 AlGaN/$In_xGa_{1-x}N$ ヘテロ構造の成長”，第 81 回応用物理学会秋季学術講演会，オンライン開催 (2020 年 9 月 10-13 日).

14. 上殿明良，上野　航，細井卓治，Egger Werner，Hugenschmidt Christoph，Dickmann Marcel，渡部平司，“陽電子消滅による GaN 基板上に成膜した TEOS-SiO_2 膜の空隙の検出” 第 81 回

応用物理学会秋季学術講演会, オンライン開催 (2020 年 9 月 10 日).

15. 嶋　紘平, 正直花奈子, 上杉謙次郎, 小島一信, 上殿明良, 三宅秀人, 秩父重英, “高温アニールスパッタ AlN 上に MOVPE 成長させた AlN の陰極線蛍光評価(1)”, 第 81 回応用物理学会秋季学術講演会, オンライン開催 (2020 年 9 月 10-13 日).

16. 粕谷拓生, 嶋　紘平, 正直花奈子, 上杉謙次郎, 小島一信, 上殿明良, 三宅秀人, 秩父重英, “高温アニールスパッタ AlN 上に MOVPE 成長させた AlN の陰極線蛍光評価(2)”, 第 81 回応用物理学会秋季学術講演会, オンライン開催 (2020 年 9 月 10-13 日).

17. M. Muralidharan, S. Sellaiyan, A. Uedono, K. Sivaji, M. Avinash, A. Kumari, “Investigation on vacancy type defects in Fe doped $SrSnO_3$ perovskite nanostructures by Positron annihilation spectroscopy”, Int. Work. Positron Study Defects, on-line (Mar. 3, 2021).

18. T. Kasuya, K. Shima, K. Shojiki, K. Uesugi, K. Kojima, A. Uedono, H. Miyake, S. F. Chichibu, “Cathodoluminescence studies of AlN epilayers grown by MOVPE on sputtered AlN templates annealed at high temperature”, 8th Asian Conf. Cryst. Growth and Cryst. Tech., On-line (Mar. 1-3, 2021).

19. A. Uedono, K. Shojiki, K. Uesugi, S. F. Chichibu, S. Ishibashi, M. Dickmann, W. Egger, C. Hugenschmidt, H. Miyake, “Vacancies in AlN deposited by radio-frequency sputtering and MOVPE studied by positron annihilation spectroscopy”, 8th Asian Conf. Cryst. Growth and Cryst. Tech., On line (Mar. 1-3, 2021).

20. M. Sumiya, Y. Takahara, A. Alghamdi, G. Andersson, A. Uedono, Y. Imanaka, “Growth of $Al_xGa_{1-x}N/In_yGa_{1-y}N$ hetero structure on AlN/sapphire templates”, 8th Asian Conf. Cryst. Growth and Cryst. Tech., On-line (Mar. 1-3, 2021).

21. 冨田啓介, 小沢　顕, 森口哲朗, 向井もも, 大和良広, 景澤怜央,”^{29}P の核磁気モーメントの符号測定”, 日本物理学会 2020 年秋季大会, オンライン開催 (2020 年 9 月 14-17 日).

22. S. Tomita, Y. Shiina, R. Suganuma, M. Matsuda, M. Imai, M. Sataka, K. Sasa, “The threshold foil thickness for the disappearance of the vicinage effect on the convoy-electron yield”, 第 21 回「イオンビームによる表面・界面の解析と改質」特別研究会, 京都大学宇治キャンパス, 現地会場とオンラインのハイブリッド形式開催　(2020 年 12 月 4-5 日).

23. 東　史弥, 谷本久典, “Fe-Mn 系反強磁性合金の圧延・焼鈍による組織変化とエリンバー特性”、2020 年日本金属学会秋期講演会, オンライン開催 (2020 年 9 月 17 日).

24. 東　史弥, 喜多英治, 谷本久典,“Fe-Mn 系反強磁性合金のエリンバー特性と組織および磁性”、2021 年日本金属学会春期講演会, オンライン開催 (2021 年 3 月 18 日).

25. 菅澤佳世，三宅芙沙，多田悠馬，堀内一穂，大谷　昴，笹　公和，高橋　努，松村万寿美，落合悠太，望月優子，高橋和也，中井陽一，本山秀明，松崎浩之，“約 100 年分のドームふじアイスコア中 ^{10}Be と ^{36}Cl の高分解能測定による BC5480 年宇宙線イベントの調査”，第 81 回応用物理学会秋季学術講演会, オンライン開催 (2020 年 9 月 8-11 日).

26. 大石脩人, 村尾吉輝, 新田紀子, 土田秀次, 冨田成夫, 笹　公和, 平田浩一，柴田裕実, 平野貴美, 山田圭介, 千葉敦也, 斎藤勇一, 鳴海一雅, 星野　靖, “C_{60}クラスターイオンビーム照射による Si 表面構造の形成”, 第 81 回応用物理学会秋季学術講演会, オンライン開催 (2020 年 9 月 8-11 日).

27. 笹　公和，高橋　努，松村万寿美，“^{36}Cl の加速器質量分析における妨害同重体 ^{36}S の除去方法の検討”, 第 81 回応用物理学会秋季学術講演会, オンライン開催 (2020 年 9 月 8-11 日).

28. 笹　公和, 石井　聡，高橋　努，大和良広，　田島義一，松村万寿美，森口哲朗，“筑波大学タンデム加速器施設の現状報告”, オンライン開催 第 17 回日本加速器学会年会 (2020 年 9 月 2-4 日).

29. 黒澤正紀，笹　公和，石井　聡，“対馬花崗岩の流体包有物中のニッケル”，日本鉱物科学会 2020 年年会, オンライン開催 (2020 年 9 月 16-17 日).

30. 小林　成, 杉澤悠紀, 岸　奈津子, 西尾和記, 関場大一郎, 清水亮太, 一杉太郎，“清浄な全固体 Li 電池界面のイオンビーム観察”，日本表面真空学会学術講演会年会，　オンライン開催 (2020 年 11 月 19-21 日).

31. N. Oishi, Y. Murao, N. Nitta, H. Tsuchida, S. Tomita, K. Sasa, K. Hirata, H. Shibata, Y. Hirano, K. Yamada, A. Chiba, Y. Saitoh, K. Narumi, Y. Hoshino, “Energy dependence of nanostructure formation by fast C_{60} cluster ion beam on Si”, 第 21 回「イオンビームによる表面・界面の解析と改質」特別研究会, 京都大学宇治キャンパス, 現地会場とオンラインのハイブリッド形式開催　(2020 年 12 月 4-5 日).

32. 笹　公和，山崎明義，石井　聡，冨田成夫，左高正雄，楢本　洋，工藤　博，“構造材料用マイクロビーム装置における多元素同時分析のためのイオンビーム分析システム”, 2021 年第 68 回応用物理学会春季学術講演会, オンライン開催 (2021 年 3 月 16-29 日).

33. 脇山義史，松村万寿美，松中哲也，平尾茂一，笹　公和，“阿武隈川における出水時の ^{129}I の挙動”, 第 7 回福島大学環境放射能研究所成果報告会, コラッセふくしま

(2021 年 3 月 18 日).

34. 中村　司, 山﨑　信哉, 石井　聰, 冨田成夫, 左高正雄, 楢本洋, 工藤　博, 笹　公和, 末木啓介, “マイクロビーム PIXE による福島第一原子力発電所事故で放出した放射性粒子の元素分布測定”, 第 22 回「環境放射能」研究会, オンライン開催 (2021 年 3 月 10-12 日).

35. 松本翔汰, 阪上朱音, 関屋涼平, 辻崚太郎, 板橋健太, 上坂友洋, 西　隆博, 銭廣十三, 矢向謙太郎, 森口哲朗, ”高精度パイ中間子原子分光・二重ガモフ―テラー巨大共鳴探索実験のための新 MWDC の開発”, 日本物理学会第 76 回年次大会, オンライン開催 (2021 年 3 月 13 日).

36. 木村容子, 三原基嗣, 松多健策, 福田光順, 大谷優里花, 高山　元, 泉川卓司, 野口法秀, 生越瑞揮, 佐藤弥紗, 高津和哉, 大坪隆, 髙橋弘幸, 百田佐多生, 奥村寛之, 森口哲朗, 小沢顕, 北川敦志、佐藤眞二, “ハルバッハ配列磁石を用いた小型 β-NMR 装置の開発”, 令和 2 年度京大複合研専門研究会「短寿命 RI を用いた核分光と核物性研究 VII」, オンライン開催 (2021 年 1 月 15 日).

37. 木村容子, 三原基嗣, 松多健策, 福田光順, 大谷優里花, 高山　元, 泉川卓司, 野口法秀, 生越瑞揮, 佐藤弥紗, 高津和哉, 大坪　隆, 髙橋弘幸, 百田佐多生, 奥村寛之, 森口哲朗, 小沢　顕, 北川敦志, 佐藤眞二, “ハルバッハ配列磁石を用いた小型 β-NMR 装置の開発”, 日本物理学会第 76 回年次大会, オンライン開催 (2021 年 3 月 12-15 日).

7.4 UTTAC seminars

2021. 1. 13 Search for baryon bound state by correlation function measurement using Λ and Ξ particles in $\sqrt{s_{NN}} = 200$ GeV Au+Au collision at RHIC-STAR experiment, *Moe Isshiki* (*University of Tsukuba*)

2021. 1. 13 Verification of nuclear theoretical model and extraction of optimum parameters using unified framework (JETSCAPE) that describes high-energy nuclear collision events, *Naoto Ito* (*University of Tsukuba*)

2021. 1. 13 Measurements of global polarization of Lambda hyperons in Au+Au collisions at $\sqrt{s_{NN}} = 3.0, 7.2, 54.4$ GeV with RHIC-STAR experiment, *Kosuke Okubo* (*University of Tsukuba*)

2021. 1. 13 Centrality determination with the Event Plane Detector and measurements of higher order cumulants of net-proton distributions in Au+Au collisions at $\sqrt{s_{NN}} = 27$ GeV from STAR, *Yuri Sato* (*University of Tsukuba*)

2021. 1. 13	Measurement of the sign of nuclear moment for unstable nuclei ^{29}P, ^{25}Al by using rotating magnetic field, *Keisuke Tomita* (*University of Tsukuba*)
2021. 1. 15	Measurement of electron v2 from bottom quark in Pb-Pb collisions at 5.02 TeV at LHC-ALICE experiment, *Yuku Sudo* (*University of Tsukuba*)
2021. 1. 15	Performance evaluation of Multi-gap Resistive Plate Chamber (MRPC) for time-of-flight detector in J-PARC E16 experiment and development of new MRPC, *Kosuke Tsukui* (*University of Tsukuba*)
2021. 1. 15	Centrality determination using Event Plane Detector in $\sqrt{s_{NN}} = 27$ GeV Au-Au collisions at RHIC-STAR experiment, *Ryoma Nakazato* (*University of Tsukuba*)
2021. 1. 15	Measurement of Full Jet using track detectors and electromagnetic calorimeters in p-p collision at 13TeV at LHC-ALICE experiment, *Keisuke Yasaki* (*University of Tsukuba*)
2021. 1. 15	Measurements of directed flow in $\sqrt{s_{NN}} = 19.7$ GeV Au-Au collision at RHIC-STAR experiment, *Taichi Ichisawa* (*University of Tsukuba*)

8.

THESES

Master theses

Keisuke Tomita	Measurement of the sign of nuclear moment for unstable nuclei ^{29}P, ^{25}Al by using rotating magnetic field (回転磁場を利用した不安定核^{29}P, ^{25}Alの核磁気モーメントの符号測定)
Sota Yamada	Magnetic Properties and Synthesis of Ferrite Nanoparticles with an Acicular Core-shell Structure (針状コア/シェル構造を持つスピネルフェライトナノ粒子の合成と特性評価)
Fumiya Higashi	Texture, Elasticity and Magnetism of Fe-Mn Based Ternary Elinvar Alloys (FeMn基３元系エリンバー合金の組織と磁気及び弾性特性)
Masato Inoue	Analysis of Vacancy-type Defects in BN Using Positron Annihilation Spectroscopy (陽電子消滅法を用いたBNの空孔型欠陥の評価)
Ryuta Yaguchi	Analysis of Vacancy-type Defects in CuMn Using Positron Annihilation Spectroscopy (陽電子消滅法によるCuMn内空孔型欠陥の評価)
Yuhki Takahara	Fabrication of AlGaN/GaN Hetero-structure on AlN Template for GaN-HEMT Device Application (GaN-HEMTデバイスに向けたAlNテンプレート上AlGaN/GaNヘテロ構造の作製)
Yuhta Kurosaki	Study of Influential Factors of High-Temperature Annealing on Electrode/n-type AlN Interface Structure (高温熱処理による電極/ｎ型AlN界面構造への影響に関する研究)

Undergraduate theses

Takehiro Okamoto	ASSESSING THE FEASIBILITY OF A LOW ORBIT LORA RELAY SATELLITE (低軌道LoRa中継衛星のフィージビリティ評価）
Mika Hayashi	Measurements of ejectile particles from arc plasma deposition source (アークプラズマ蒸着源からの出射粒子の測定）
Asahi Yano	Study of $\vec{\mathrm{p}} + {}^{\mathrm{nat.}}\mathrm{Si}$ reaction in UTTAC 6MV tandem accelerator (UTTAC 6MVタンデム加速器における$\vec{\mathrm{p}} + {}^{\mathrm{nat.}}\mathrm{Si}$反応の研究）
Ginga Kawasaki	Depth and lateral resolution of transmission ERDA analysis for the three dimensional distribution of hydrogen in aluminum (透過型ERDAを用いたAl中3次元水素分析の分解能評価）
Souta Hatada	Development of two-dimensional data acquisition system of time of flight and pulse height using FPGA (FPGAボードを用いた飛行時間-波高2次元計測システムの開発）

Tsukasa Nakamura	Element distributions of radioactive particles emitted in the Fukushima Daiichi Nuclear Power Plant accident by microbeam PIXE (マイクロビーム PIXE による福島第一原子力発電所事故で放出された放射性粒子の元素分布測定）
Akane Taira	Fabrication of Ionization Chamber for TOF-E telescope ERDA (TOF-E telescope ERDA 用電離箱の製作）

9.

LIST OF PERSONNEL

Tandem Accelerator Complex

A. Uedono	Director, Professor
K. Sasa	Associate Professor
D. Sekiba	Lecturer
T. Moriguchi	Assistant Professor
Y. Tajima	Mechanical Engineer
S. Ishii	Mechanical Engineer
T. Takahashi	Electrical Engineer
Y. Yamato	Electrical Engineer
M. Matsumura	Technical Staff
S. Kuramochi	Administrative Staff
K. Iwase	Administrative Staff
H. Muromachi	Administrative Staff

Research Members[1]

Department of Physics

A. Ozawa K. Sasa T. Moriguchi

T. Yamaguchi (Saitama University [Cross appointment])

Department of Applied Physics

A. Uedono H. Yanagihara H. Tanimoto E. Kita

S. Tomita D. Sekiba S. Sharmin

Department of Geoscience

M. Kurosawa

Department of Biology

I. Suzuki

Department of Chemistry

K. Sueki A. Sakaguchi

Department of Information and Systems

T. Kameda

---

[1] The “research members” include the authors and coauthors within 5 years back from this fiscal year, as well as the members of research projects running at UTTAC.

Staff of Open Advanced Facilities Initiative

H. Kudo
H. Naramoto
M. Sataka
K. Awazu (National Institute of Advanced Industrial Science and Technology [AIST])
S. Aoki (Comprehensive Research Organization for Science and Society [CROSS])

Graduate students

Y. Sugisawa
D. Hirose
Z. Shi
M. Inoue
K. Tomita
N. Kishi
D. Shiine
R. Yaguchi
N. Kaname
K. Nishizuka
T. Yang
F. Higashi
S. Yamada
Y. Gao
T. Ikeda

Undergraduates

M. Hayashi
S. Hatada
A. Yano
T. Okamoto
A. Taira
T. Nakamura
G. Kawasaki

External users and collaborators

Y. Iwata	National Institute of Advanced Industrial Science and Technology (AIST)
K. Tomita	National Institute of Advanced Industrial Science and Technology (AIST)
S. Shiki	National Institute of Advanced Industrial Science and Technology (AIST)
T. Ishizuka	National Institute of Advanced Industrial Science and Technology (AIST)
T. Matsunaka	Kanazawa University
M. Mihara	Osaka University
Y. Otani	Osaka University
Y. Kimura	Osaka University
H. Ishiyama	RIKEN
S. Matsumoto	Kyoto University, RIKEN
A. Sakaue	RIKEN
K. Itahashi	RIKEN
T. Uesaka	RIKEN
J. Zenihiro	Kyoto University
K. Yako	University of Tokyo
R. Sekiya	Kyoto University, RIKEN
R. Tsuji	Kyoto University
Y. Shiina	Rikkyo University
F. Miyake	Nagoya University
K. Kanzawa	Nagoya University